

Molecular Clouds at the Edge of the Galaxy

I. Variation of CO $J=2-1/1-0$ Line Ratio

C. S. Luo^{1,2}, X. D. Tang^{1,2,3,4}, C. Henkel^{5,1}, K. M. Menten⁵, Y. Sun⁶, Y. Gong^{6,5}, X. W. Zheng⁷, D. L. Li^{1,2,4}, Y. X. He^{1,2,4}, X. Lu⁸, Y. P. Ao⁶, X. P. Chen⁶, T. Liu⁸, K. Wang⁹, J. W. Wu^{10,2}, J. Esimbek^{1,3,4}, J. J. Zhou^{1,3,4}, J. J. Qiu¹¹, X. Zhao^{1,2}, J. S. Li^{1,2}, Q. Zhao^{1,2}, and L. D. Liu^{1,2}

¹ Xinjiang Astronomical Observatory, Chinese Academy of Sciences, Urumqi 830011, PR China
e-mail: tangxindi@xao.ac.cn

² University of the Chinese Academy of Sciences, Beijing 100080, PR China

³ Key Laboratory of Radio Astronomy and Technology, Chinese Academy of Sciences, A20 Datun Road, Chaoyang District, Beijing 100101, PR China

⁴ Xinjiang Key Laboratory of Radio Astrophysics, Urumqi 830011, PR China

⁵ Max-Planck-Institut für Radioastronomie, Auf dem Hügel 69, 53121 Bonn, Germany

⁶ Purple Mountain Observatory, Chinese Academy of Sciences, Nanjing 210008, PR China

⁷ School of Astronomy and Space Science, Nanjing University, Nanjing 210093, PR China

⁸ Shanghai Astronomical Observatory, Chinese Academy of Sciences, 80 Nandan Road, Shanghai 200030, PR China

⁹ Kavli Institute for Astronomy and Astrophysics, Peking University, Beijing 100871, PR China

¹⁰ National Astronomical Observatories, Chinese Academy of Sciences, Beijing 100101, PR China

¹¹ School of Mathematics and Physics, Jinggangshan University, Ji'an 343009, PR China

April 21, 2025

ABSTRACT

The Galactic edge at Galactocentric distances of 14–22 kpc provides an ideal laboratory to study molecular clouds in an environment that is different from the solar neighborhood, due to its lower gas density, lower metallicity, and little or no perturbation from the spiral arms. Observations of CO ($J=2-1$) spectral lines were carried out towards 72 molecular clouds located at the Galactic edge using the IRAM 30 m telescope. Combined with CO ($J=1-0$) data from the MWISP project, we investigate the variations of R_{21} across these Galactic edge clouds, with R_{21} representing CO(2-1)/CO(1-0) integrated intensity ratios. These are found to range from 0.3 to 3.0 with a mean of 1.0 ± 0.1 in the Galactic edge clouds. The proportions of very low ratio gas (VLRG; $R_{21} < 0.4$), low ratio gas (LRG; $0.4 \leq R_{21} < 0.7$), high ratio gas (HRG; $0.7 \leq R_{21} < 1.0$), and very high ratio gas (VHRG; $R_{21} \geq 1.0$) are 6.9%, 29.2%, 26.4%, and 37.5%, respectively, indicating a significant presence of high R_{21} ratio molecular gas within these regions. In our Galaxy, the R_{21} ratio exhibits a gradient of initial radial decline followed by a high dispersion with increasing Galactocentric distance and a prevalence for high ratio gas. There is no apparent systematic variation within the Galactocentric distance range of 14 to 22 kpc. A substantial proportion of HRG and VHRG is found to be associated with compact clouds and regions displaying star-forming activity, suggesting that the high R_{21} ratios may stem from dense gas concentrations and recent episodes of star formation.

Key words. stars: formation – ISM: clouds – ISM: molecules – radio lines: ISM

1. Introduction

1.1. Galactic edge clouds

The outer regions of the Galaxy offer a unique laboratory to investigate the influence of metallicity on star formation, with a spatial resolution that allows for the identification and classification of individual clumps and cores within giant molecular clouds (GMCs). Compared to nearby clouds, little is known about molecular clouds at the edge of the Galaxy lying farther than ~ 14 kpc from the Galactic center. This is primarily due to the difficulty encountered in undertaking carbon monoxide (CO) surveys that are sensitive, unbiased, and cover a large area (Digel et al. 1994). The outer Galaxy may be younger than the regions farther inside (Martig et al. 2016). The edge of the Galaxy appears to have a relatively shorter and less complex history of star formation, attributed to its lower gas density, lower metallicity, and minimal perturbation from the spiral arms (e.g., Smartt & Rolleston 1997; Heyer & Dame 2015; Wenger et al. 2019; Lian

et al. 2023; Urquhart et al. 2024). Consequently, this region provides an ideal laboratory to study the process of star and stellar cluster formation without the complications arising from intertwined star formation activity in both space and time.

Various surveys of molecular lines (e.g., CO, CS, OH, HCO⁺, HCN, H₂O, H₂CO, NH₃, CH₃OH) in the outer Galaxy have been carried out (e.g., Mead & Kutner 1988; Wouterloot & Brand 1989; Wouterloot et al. 1993; Brand & Wouterloot 1994; Heyer et al. 1998; Pirogov 1999; Snell et al. 2002; Ruffle et al. 2007; Blair et al. 2008; Dame & Thaddeus 2011; Sun et al. 2015, 2018b; Wang et al. 2018; Braine et al. 2023; Koelemay et al. 2023). These surveys indicate that the molecular disk of our Galaxy extends beyond 20 kpc from the Galactic center. The star formation process has been studied in the extreme outer Galaxy, which differs significantly from that of the solar neighborhood environment (e.g., Digel et al. 1994; Brand & Wouterloot 1995, 2007; Wouterloot & Brand 1996; Snell et al. 2002; Yasui et al. 2006, 2008; Ruffle et al. 2007; Kobayashi et al. 2008;

Izumi et al. 2014, 2017, 2022, 2024; Armentrout et al. 2017; Matsuo et al. 2017; Sun et al. 2017, 2024a,b; Shimonishi et al. 2021; Bernal et al. 2021; Braine et al. 2023; Urquhart et al. 2024; Lin et al. 2025). However, the process of star formation in such environments has not been as extensively studied as in nearby star-forming regions due to their considerable heliocentric distances.

Recently, Dame & Thaddeus (2011) and Sun et al. (2015) identified a new segment of a spiral arm situated beyond the outer arm in both the first Galactic quadrant ($13^\circ < l < 55^\circ$) and the second Galactic quadrant ($100^\circ < l < 150^\circ$) (see Fig. 1). A large number of molecular clouds have been identified on the new arm, which is located approximately 14–22 kpc from the Galactic center (Dame & Thaddeus 2011; Sun et al. 2015). These Galactic edge clouds present an optimal opportunity for investigating the properties and chemistry of molecular gas in the extreme outer Galaxy. Presently, the study of these molecular clouds still has been poor on basic properties, such as size, density, temperature, and star formation. A comprehensive investigation of the Galactic edge clouds will illuminate our comprehension of star formation within low-metallicity environments. Consequently, high-sensitivity CO observations with suitable angular resolutions are crucial for determining physical parameters. This will establish an observational basis for subsequent studies of rarer molecular tracers in the extreme outer Galaxy.

1.2. CO as a probe of physical conditions

CO stands as the second most abundant molecular species, only following molecular hydrogen (H_2), and has consequently been employed as a reliable indicator of molecular gas. It is usually used to trace the variety of physical conditions of the bulk molecular gas (e.g., Bolatto et al. 2013; Peñaloza et al. 2017, 2018). The two primary rotational transitions of the dominant CO molecule, $^{12}C^{16}O J=1-0$ (hereafter CO(1–0)) and $^{12}C^{16}O J=2-1$ (hereafter CO(2–1)), exhibit favorable frequencies for ground-based observations. These transitions are commonly employed to trace the mass of molecular gas in galaxies. Quantitative comparison of results obtained using the CO $J=2-1/1-0$ integrated intensity ratio, denoted as R_{21} , is gaining more and more importance. The R_{21} ratio has been observed to exhibit variability in different environments. Investigations into this ratio have been conducted in a variety of molecular conditions, encompassing studies within the Milky Way (e.g., Chiar et al. 1994; Sakamoto et al. 1994, 1997; Oka et al. 1998; Seta et al. 1998; Handa et al. 1999; Sawada et al. 2001; Salomé et al. 2008; Yoda et al. 2010; Zhang et al. 2019) and nearby galaxies (e.g., Braine & Combes 1992; Sorai et al. 2001; Bolatto et al. 2003; Leroy et al. 2009, 2022; Koda et al. 2012, 2020; Zschaechner et al. 2018; den Brok et al. 2021; Yajima et al. 2021; Maeda et al. 2022; Liu et al. 2023; Keenan et al. 2025). Through numerical simulations, it has been demonstrated that the R_{21} effectively constrains the physical conditions of molecular gas, such as density, temperature, and optical depth (e.g., Goldsmith et al. 1983; Castets et al. 1990; Sakamoto 1994; Sakamoto et al. 1997; Koda et al. 2012; Zhang et al. 2019; Schinnerer & Leroy 2024). Therefore, understanding the variations of R_{21} perhaps in response to the ambient environment also holds the potential to yield valuable insights into the physical conditions of the molecular gas. Molecular gas can be categorized into four distinct groups based on the R_{21} value using a large velocity gradient (LVG) approximation (Sakamoto et al. 1997) in the following way:

- Very low ratio gas (VLRG) corresponds to cases where $R_{21} < 0.4$. The faint VLRG is typically undetectable with observations of low sensitivity. Nevertheless, Lindt-Krieg et al. (2008) identified a CO line ratio of ~ 0.3 , suggesting the presence of cold or sub-thermally excited gas within the overall galaxy host.
- Low ratio gas (LRG) is observed for $0.4 \leq R_{21} < 0.7$. The excitation of the LRG has been demonstrated to be characterized by diffuse gas and/or gas of low kinetic temperatures. Measurements of R_{21} indicate values of ~ 0.5 for peripheral regions and ~ 0.6 for intermediate regions in the Orion giant molecular cloud (Sakamoto 1994). The presence of the LRG is not confined solely to the disk and molecular ring of the Milky Way (Chiar et al. 1994; Sawada et al. 2001). It has also been detected in the interarm regions of galaxies (e.g., Koda et al. 2012, 2020) and nearby star-forming galaxies (e.g., den Brok et al. 2021; Yajima et al. 2021; Leroy et al. 2022; Maeda et al. 2022).
- High ratio gas (HRG) is defined as having a ratio of $0.7 \leq R_{21} < 1.0$. The excitation of the HRG is primarily due to collisions within local thermodynamic equilibrium (LTE), owing to the density and elevated temperature of the gas (Sakamoto 1994). This type of molecular characteristics has been found in the Large Magellanic Cloud (LMC) (e.g., Sorai et al. 2001), as well as in the central regions of normal star-forming galaxies (e.g., Sawada et al. 2001; Leroy et al. 2009; Koda et al. 2012) and the spiral arm regions of nearby galaxies (e.g., Wiklind et al. 1990; Koda et al. 2012, 2020).
- Very high ratio gas (VHRG) with values $R_{21} \geq 1.0$: The presence of VHRG is unexpected in instances of optically thick emission. Instead, it is typically found in either warm ($T_{\text{kin}} \gtrsim 50$ K), dense ($n_{H_2} \gtrsim 3 \times 10^3 \text{ cm}^{-3}$), and optically thin, or externally heated gas (Sakamoto et al. 1997). This gas has been detected in the vicinity of Orion KL (Nishimura et al. 2015), and within the N83/N84 molecular cloud complex situated inside the Small Magellanic Cloud (SMC) (Bolatto et al. 2003). Additionally, it has been identified in metal-poor galaxies such as NGC 3310 (Braine & Combes 1992) and NGC 1140 (Hunt et al. 2017).

As stated previously, R_{21} exhibits consistent variations both within the Milky Way and across different galaxies, serving as an indicator of molecular gas conditions. Consequently, it is plausible that estimations of molecular gas mass, as well as related quantities and relationships derived from CO $J=2-1$ assuming a constant $R_{21} \sim 0.7$ (e.g., Sandstrom et al. 2013; Sun et al. 2018a; König et al. 2021), may be subject to misinterpretation. It is also crucial to acknowledge the existing uncertainty surrounding the CO-to- H_2 conversion factor. Therefore, it is advisable to conduct thorough examinations to validate the assumption of R_{21} constancy and assess its impact on derived quantities and relationships pertaining to molecular gas.

To date, a comprehensive measurement of the R_{21} ratio in molecular clouds situated beyond 14 kpc at the Milky Way's periphery remains unexplored. Hence, this investigation is particularly significant for numerous molecular clouds situated in the second Galactic quadrant at the edge of the Galaxy. We aim to explore the underlying causes of R_{21} variations in conjunction with the physical properties of molecular gas. In Sects. 2 and 3, we introduce our targets, observations, data reduction, and describe the main results. The discussion of resulting R_{21} ratios is presented in Sect. 4. Our main conclusions are summarized in Sect. 5. This paper is part of the "Molecular Clouds at the Edge of the Galaxy" project, which focuses on the investigation of the

physical and chemical properties of molecular clouds and star formation located in the outskirts of the Milky Way.

2. Targets, observations, and data reduction

2.1. Targets

We selected 72 Galactic edge clouds with masses on the order of 10^2 – $10^4 M_\odot$ spanning the Galactic longitude range of $100^\circ < l < 150^\circ$ from the Milky Way Imaging Scroll Painting (MWISP) project¹ (see Fig. 1; Sun et al. 2015). This project is an unbiased northern Galactic plane CO survey conducted using the Delingha 13.7 m telescope (Su et al. 2019). These Galactic edge clouds exhibit a wide range of Galactocentric radii, spanning approximately 14 to 22 kpc, with a median equivalent radius of 17 kpc (kinematic distance; Sun et al. 2015). Typical radial velocity of these Galactic edge clouds is $-102 \pm 10 \text{ km s}^{-1}$. Masses and sizes of these Galactic edge clouds are relatively small compared to the molecular clouds in the inner Galaxy (Solomon et al. 1987; Heyer et al. 2009). The H_2 column density of the dense clumps in these Galactic edge clouds ranges from 5×10^{20} to $3.6 \times 10^{21} \text{ cm}^{-2}$. While over ten clouds clearly show ^{13}CO (1–0), a considerable number of other clouds were only marginally detected in this line, lacking a notable C^{18}O (1–0) feature (Sun 2015). The structure of nine molecular clouds in these poorly studied subsolar metallicity regions and their relation with star formation have been investigated using the dense gas tracers HCN (1–0) and HCO^+ (1–0) (Braine et al. 2023). Evidence of star formation within Galactic edge clouds is apparent (Sun 2015). Out of their 26 molecular clouds, a correlation with young stellar objects (YSOs) has been identified. Within this subset, 34 molecular cores are associated with YSOs. Furthermore, stellar clusters have been discovered in Digel Cloud 1 and 2 (e.g., Yasui et al. 2006; Ruffle et al. 2007; Kobayashi et al. 2008; Izumi et al. 2014), specifically in G131.016+1.524, G131.157+1.390, G137.759–0.983, and G137.775–1.067. These findings suggest widespread star formation even within the extreme outer Galaxy.

2.2. Observations of CO (2–1)

The observations were conducted using the Institut de Radioastronomie Millimétrique 30 m diameter (IRAM 30 m) telescope² at Pico Veleta Observatory. Sky opacity at the telescope site varied from 0.2 to 0.4 at 2 mm, with fluctuations observed over the course of the measurements³. The pointing accuracy of the telescope was better than $3''$. Pointing checks were conducted every 1 to 2 hours to ensure precision. Our CO (2–1) observations were carried out in December 2015, January 2016, and April 2016 utilizing the multibeam HETERODYNE Receiver Array (HERA). HERA possesses the capability to efficiently observe nine positions on the sky simultaneously with dual-polarization. At a central frequency of $\sim 230 \text{ GHz}$, the main parameters include a Half Power Beam Width (HPBW) of $\sim 11''$, a main beam efficiency of ~ 0.59 , a forward efficiency of ~ 0.92 , and a system noise temperature of $\sim 500 \text{ K}$ (T_A^* scale). The backend spectrometer, with 5377 spectral channels and an aggregate bandwidth of $\sim 1 \text{ GHz}$, provides a frequency resolution of 200 kHz, corresponding to a channel width of $\sim 0.25 \text{ km s}^{-1}$ at a frequency of $\sim 230 \text{ GHz}$. We employed the On-The-Fly (OTF) observing mode to generate seventy-two maps ($\sim 100'' \times 100''$) with steps of $3''.5$ in

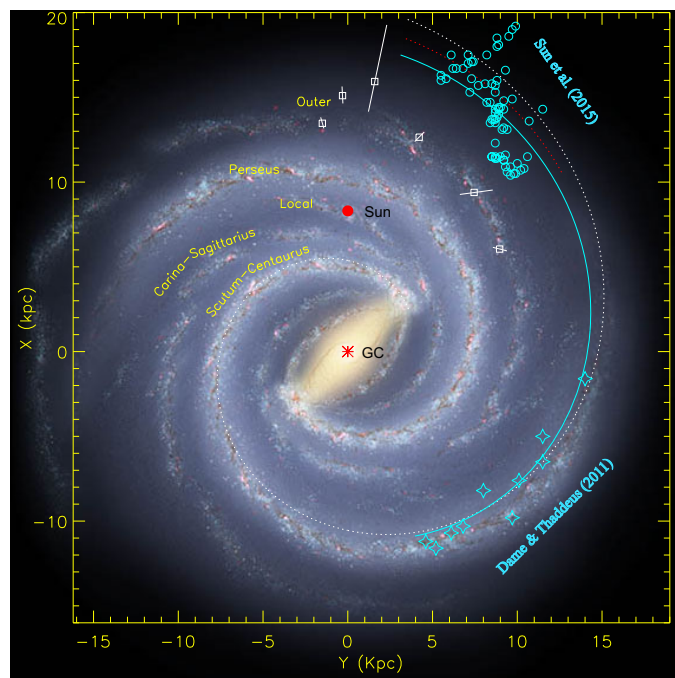


Fig. 1. Locations of 72 selected molecular clouds in the far outer Galaxy (marked by cyan circles). Locations of the high-mass star forming regions associated with the Outer Arm are denoted by white squares, with crossing white lines indicating distance uncertainties (Reid et al. 2014). The white dashed line traces a log spiral with a mean pitch angle of 12° that was fit to the Scutum–Centaurus arm. The red dashed line traces the log-periodic spiral that is fitting results to clouds ($120^\circ < l < 150^\circ$) detected by Sun et al. (2015). The cyan solid line traces the log-periodic spiral fitting results to clouds detected by Dame & Thaddeus (2011) and Sun et al. (2015). Image adapted from Sun et al. (2015).

both right ascension and declination. The central positions of the CO (2–1) observations in the 72 Galactic edge clouds are determined by identifying peaks in the CO (1–0) emission from the Delingha 13.7 m telescope (see Fig. A.1; Sun et al. 2015). The typical root-mean-square (RMS) noise levels for the CO (2–1) data are ~ 0.3 – 0.5 K (T_{mb} scale) at a channel width of $\sim 0.25 \text{ km s}^{-1}$. The observed sources are listed in Table 1.

2.3. Archival data of CO (1–0)

CO (1–0) data were procured as part of the MWISP project (Sun et al. 2015). The Delingha 13.7 m telescope is equipped with a 3×3 multibeam sideband-separation Superconducting Spectroscopic Array Receiver (SSAR), operating within a frequency range of 85–115 GHz (Shan et al. 2012). The average zenith opacity is around 0.2 at 115 GHz⁴. The typical system temperature for CO (1–0) is 250–300 K (T_A^* scale). The pointing accuracy is better than $5''$, while the tracking error is approximately $1''$ – $3''$. The MWISP observations encompass simultaneous measurements of ^{12}CO , ^{13}CO , and C^{18}O (1–0) lines, utilizing the OTF mode. The sampling interval is set at $15''$, which is equivalent to the scan rate ($50'' \text{ s}^{-1}$) multiplied by the dump time (0.3 s) in observations. The HPBW, the main beam efficiency, and the typical RMS noise level for CO (1–0) are approximately $52''$, 0.46, and 0.5 K, respectively. The backend instrumentation, utilizing a Fast Fourier Transform Spectrometer (FFTS), is configured with a 1 GHz bandwidth and 16384 spectral channels, yielding a spectral resolution of 61 kHz and a channel width of

¹ <http://www.radioast.nsd.c.cn/english/mwisp.php>

² Based on observations obtained with the IRAM 30 m telescope. IRAM is supported by INSU/CNRS (France), MPG (Germany), and IGN (Spain).

³ <https://publicwiki.iram.es/TelescopeSystemStatus>

⁴ <http://english.dlh.pmo.cas.cn/fs/>

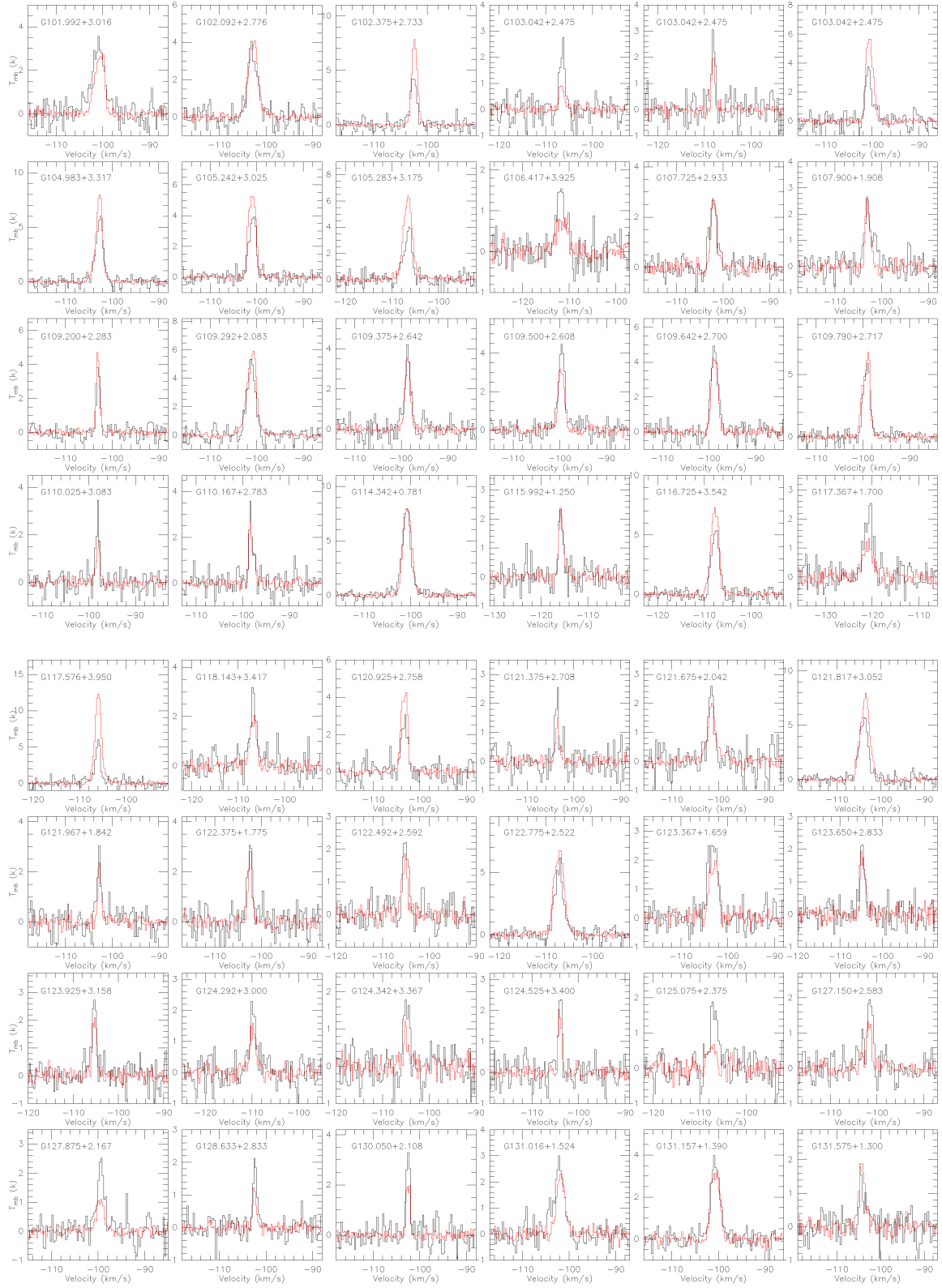


Fig. 2. The observed CO $J = 1-0$ spectra (black line) and 2-1 profiles (red line) toward the Galactic edge clouds. The CO lines were extracted from the CO (1-0) emission peaks. The CO (2-1) line cubes have been smoothed to match that of the CO (1-0) line, $52''$, for comparison.

$\sim 0.16 \text{ km s}^{-1}$ at 115 GHz. The raw data were subsequently re-gridded into $30'' \times 30''$ pixels, constituting a $30' \times 30'$ mosaic fits cube (Su et al. 2019; Ma et al. 2021).

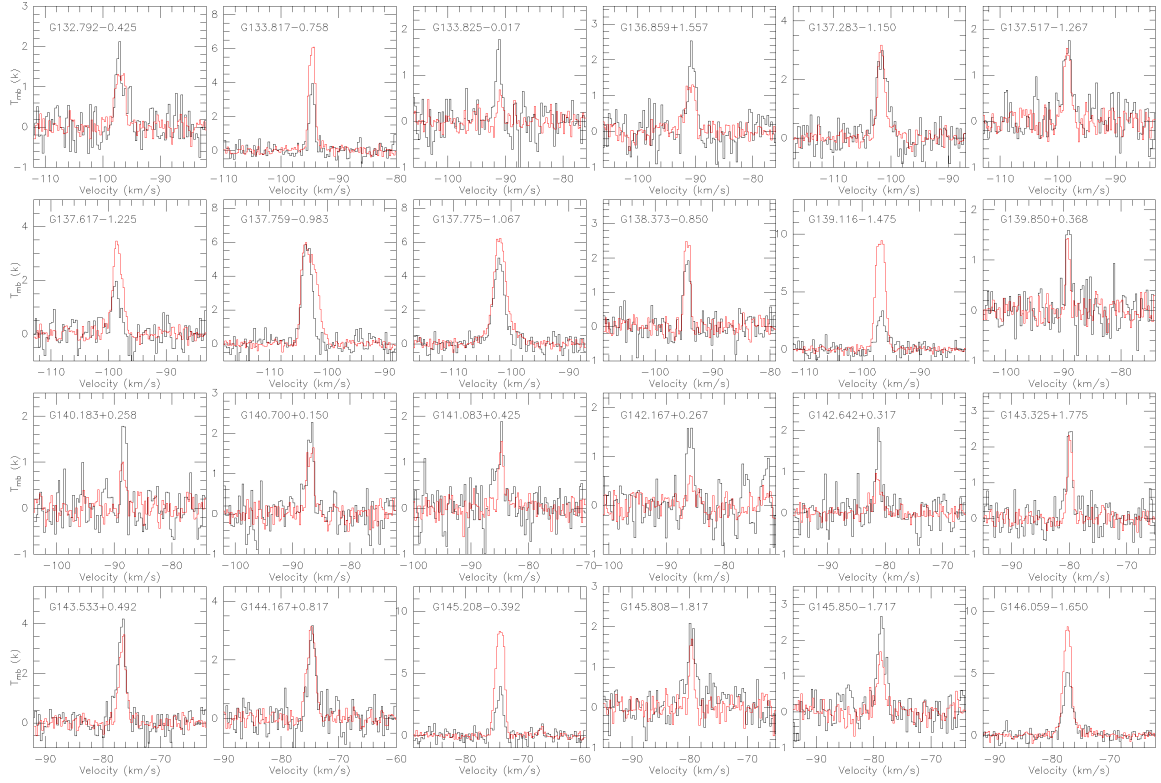


Fig. 2. continued.

2.4. Data reduction

The spectral lines were processed utilizing the GILDAS⁵ package. As a first step in this process, we removed low-quality CO(2–1) spectral lines and merged dual-polarization spectral lines to enhance the signal-to-noise ratio (S/N). The CO(1–0) spectral lines were smoothed over two consecutive channels to achieve a velocity resolution of $\sim 0.32 \text{ km s}^{-1}$, which closely aligns with the CO(2–1) channel width of $\sim 0.25 \text{ km s}^{-1}$. In order to match the spatial resolution of the CO(1–0) data, we smoothed the CO(2–1) data cube to a $52''$ resolution and resampled the spectral lines at $\sim 30''$ intervals. The parameters of the CO(2–1) spectra were only determined by aligning them with positions in the CO(1–0) peak emission and employing a Gaussian line profile for fitting, including the local standard of rest velocity (V_{LSR}), main beam brightness peak temperature (T_{mb}), full width at half maximum linewidth (ΔV), and velocity-integrated intensity ($\int T_{\text{mb}} dv$). These fitted results are listed in Table 1. The parameters for the CO(1–0) spectra are detailed in Table 1 of Sun et al. (2015).

Additionally, the heliocentric distance (d) and the Galactocentric distance (R_g) were derived from the Galactic rotation curve as outlined by Reid et al. (2014). The heliocentric distances of these Galactic edge clouds vary between approximately 9 and 15 kpc, with a mean value of $\sim 11 \text{ kpc}$ (Sun et al. 2015). Correspondingly, the spatial linear scales range from 2.3 to 3.7 pc at a beam size of $52''$, with an average of $\sim 2.8 \text{ pc}$. In this work, the CO $J=2-1/1-0$ integrated intensity ratio ($R_{21} = I_{\text{CO}(2-1)} / I_{\text{CO}(1-0)}$) was obtained for the Galactic edge clouds. Velocity ranges utilized for spectral integration are consistent across both CO transitions. All CO(1–0) main beam brightness temperatures (T_{mb}) presented in this work have

been calibrated for main beam efficiencies ($\eta_{\text{mb}} \sim 0.46$), being expressed as $T_{\text{mb}} = T_{\text{A}}^* / \eta_{\text{mb}}$, where T_{A}^* represents the antenna temperature. CO(2–1) main beam brightness temperatures have been calibrated for main beam efficiencies ($B_{\text{eff}} \sim 0.59$) and the forward hemisphere efficiency ($F_{\text{eff}} \sim 0.92$), being expressed as $T_{\text{mb}} = (F_{\text{eff}} / B_{\text{eff}}) T_{\text{A}}^*$.

3. Results

3.1. Overview

The observed CO(1–0) and (2–1) spectra are depicted in Fig. 2. The CO(2–1) lines are detected in all sources. The integrated intensity distributions of CO(2–1) for the 72 Galactic edge clouds will be detailed in Luo et al. (in prep.). Among these observed molecular clouds, 25 present compact structures⁶, 25 display diffuse structures, and 22 manifest intermediate morphologies between the two based on identification by eye (see Table 1). Typical examples of these three structures are shown in Fig. A.1. The fitted line parameters, integrated intensity, linewidth, and peak temperature of CO(1–0) and (2–1) are depicted in Fig. 3. Good correlations have been observed between these parameters. The centroid velocities for both lines are similar (see Table 1 and Table 1 in Sun et al. 2015). The linewidths of both CO(1–0) and (2–1) are notably narrow, exhibiting a similar range. For the CO(1–0) transition, the linewidth ranges from 0.7 to 3.3 km s^{-1} , with an average of $1.6 \pm 0.3 \text{ km s}^{-1}$ (errors given here and elsewhere are standard deviations of the mean). Similarly, in the

⁶ The forthcoming work by Luo et al. (in prep) will provide a detailed account of the identification of "compact" CO clumps extracted using quickclump (Sidorin 2017). The angular sizes of these CO clumps range from approximately $16''$ to $58''$, with a mean size of $\sim 27''$. In linear terms, these clumps span from 0.6 to 3.9 pc, with an average size of $\sim 1.3 \text{ pc}$.

⁵ <http://www.iram.fr/IRAMFR/GILDAS>

Table 1. CO spectral parameters.

Sources	l °	b °	d kpc	V_{LSR} km s ⁻¹	ΔV km s ⁻¹	T_{mb} K	$I_{\text{CO}(2-1)}$ K km s ⁻¹	$I_{\text{CO}(1-0)}$ K km s ⁻¹	R_{21}	Structure	SF Activity
G101.992+3.016	101.992	3.016	9.8	-100.7 ± 0.1	2.4 ± 0.1	2.8 ± 0.3	7.1 ± 0.2	10.4 ± 0.8	0.68 ± 0.06	Moderate	With
G102.092+2.776	102.092	2.776	10.1	-102.7 ± 0.1	2.4 ± 0.1	4.0 ± 0.2	10.1 ± 0.2	8.9 ± 0.6	1.13 ± 0.08	Compact	With
G102.375+2.733	102.375	2.733	10.0	-102.4 ± 0.1	1.2 ± 0.1	7.9 ± 0.1	10.2 ± 0.1	6.2 ± 0.5	1.65 ± 0.14	Compact	With
G103.042+2.475	103.042	2.475	10.5	-106.6 ± 0.1	1.3 ± 0.2	1.0 ± 0.1	1.3 ± 0.1	3.3 ± 0.4	0.39 ± 0.06	Moderate	Without
G103.458+3.300	103.458	3.300	10.7	-108.1 ± 0.1	0.7 ± 0.1	2.2 ± 0.2	1.6 ± 0.1	2.8 ± 0.4	0.57 ± 0.09	Moderate	Without
G103.729+2.867	103.729	2.867	9.7	-100.6 ± 0.1	1.8 ± 0.1	5.9 ± 0.4	11.1 ± 0.2	6.1 ± 0.6	1.82 ± 0.19	Compact	With
G104.983+3.317	104.983	3.317	9.9	-102.7 ± 0.1	1.6 ± 0.1	8.0 ± 0.4	13.7 ± 0.2	11.4 ± 0.5	1.20 ± 0.06	Compact	With
G105.242+3.025	105.242	3.025	9.6	-101.0 ± 0.1	1.8 ± 0.1	5.7 ± 0.4	10.7 ± 0.2	7.5 ± 0.4	1.43 ± 0.09	Compact	With
G105.283+3.175	105.283	3.175	10.4	-106.6 ± 0.1	2.2 ± 0.1	6.3 ± 0.2	14.6 ± 0.2	8.1 ± 0.6	1.80 ± 0.14	Compact	With
G106.417+3.925	106.417	3.925	11.1	-111.6 ± 0.2	2.8 ± 0.3	0.7 ± 0.2	2.2 ± 0.2	3.2 ± 0.5	0.69 ± 0.13	Diffuse	Possible
G107.725+2.933	107.725	2.933	9.7	-102.0 ± 0.1	1.4 ± 0.1	2.8 ± 0.2	4.2 ± 0.2	4.8 ± 0.4	0.88 ± 0.09	Moderate	Without
G107.900+1.908	107.900	1.908	9.7	-103.0 ± 0.1	1.2 ± 0.1	2.5 ± 0.3	3.3 ± 0.2	4.5 ± 0.5	0.73 ± 0.10	Moderate	Without
G109.200+2.283	109.200	2.283	9.8	-103.1 ± 0.1	0.9 ± 0.1	4.7 ± 0.1	4.4 ± 0.1	3.4 ± 0.3	1.29 ± 0.12	Compact	Without
G109.292+2.083	109.292	2.083	9.5	-101.0 ± 0.1	2.3 ± 0.1	5.8 ± 0.4	14.4 ± 0.2	11.5 ± 0.5	1.25 ± 0.06	Compact	With
G109.375+2.642	109.375	2.642	9.2	-98.6 ± 0.1	1.3 ± 0.1	3.7 ± 0.1	5.0 ± 0.2	5.9 ± 0.5	0.85 ± 0.08	Moderate	With
G109.500+2.608	109.500	2.608	9.3	-99.7 ± 0.1	1.5 ± 0.1	3.3 ± 0.2	5.2 ± 0.2	7.4 ± 0.4	0.70 ± 0.05	Moderate	Possible
G109.642+2.700	109.642	2.700	9.2	-98.9 ± 0.1	1.6 ± 0.1	4.5 ± 0.3	7.7 ± 0.2	9.1 ± 0.5	0.85 ± 0.06	Moderate	Possible
G109.790+2.717	109.790	2.717	9.2	-99.2 ± 0.1	1.9 ± 0.1	6.4 ± 0.7	13.1 ± 0.2	10.3 ± 0.5	1.27 ± 0.07	Compact	Possible
G110.025+3.083	110.025	3.083	9.1	-98.0 ± 0.1	1.0 ± 0.1	1.7 ± 0.2	1.7 ± 0.2	2.9 ± 0.3	0.59 ± 0.10	Moderate	Without
G110.167+2.783	110.167	2.783	9.1	-98.2 ± 0.1	1.2 ± 0.1	2.3 ± 0.4	2.9 ± 0.2	3.3 ± 0.4	0.88 ± 0.13	Moderate	Possible
G114.342+0.781	114.342	0.781	9.5	-100.7 ± 0.1	2.1 ± 0.1	8.1 ± 0.2	18.6 ± 0.2	18.0 ± 0.4	1.03 ± 0.03	Compact	With
G115.992+1.250	115.992	1.250	11.9	-115.8 ± 0.1	1.0 ± 0.1	2.3 ± 0.1	2.5 ± 0.2	2.6 ± 0.4	0.96 ± 0.17	Moderate	Without
G116.725+3.542	116.725	3.542	10.5	-107.8 ± 0.1	1.9 ± 0.1	7.4 ± 0.4	15.2 ± 0.2	11.3 ± 0.5	1.35 ± 0.07	Compact	With
G117.367+1.700	117.367	1.700	13.0	-121.0 ± 0.1	2.4 ± 0.2	1.1 ± 0.2	2.9 ± 0.2	5.1 ± 0.5	0.57 ± 0.07	Diffuse	Possible
G117.576+3.950	117.576	3.950	10.3	-106.0 ± 0.1	1.6 ± 0.1	12.4 ± 0.4	20.8 ± 0.2	7.7 ± 0.6	2.70 ± 0.22	Compact	With
G118.143+3.417	118.143	3.417	10.4	-106.7 ± 0.1	1.6 ± 0.1	2.0 ± 0.2	3.4 ± 0.2	4.9 ± 0.6	0.69 ± 0.10	Moderate	Without
G120.925+2.758	120.925	2.758	10.1	-103.3 ± 0.1	1.6 ± 0.1	4.4 ± 0.3	7.5 ± 0.2	4.8 ± 0.5	1.56 ± 0.17	Compact	Without
G121.375+2.708	121.375	2.708	10.2	-103.5 ± 0.1	0.9 ± 0.1	1.4 ± 0.1	1.3 ± 0.1	2.4 ± 0.4	0.54 ± 0.10	Moderate	Without
G121.675+2.042	121.675	2.042	9.9	-101.4 ± 0.1	2.0 ± 0.2	1.9 ± 0.2	4.0 ± 0.2	3.9 ± 0.5	1.03 ± 0.15	Compact	Without
G121.817+3.052	121.817	3.052	10.3	-103.6 ± 0.1	2.6 ± 0.1	7.5 ± 0.3	20.3 ± 0.2	13.7 ± 0.5	1.48 ± 0.06	Compact	With
G121.967+1.842	121.967	1.842	10.1	-102.7 ± 0.1	0.8 ± 0.1	2.4 ± 0.1	2.1 ± 0.2	3.0 ± 0.5	0.70 ± 0.14	Diffuse	With
G122.375+1.775	122.375	1.775	10.1	-102.3 ± 0.1	1.0 ± 0.1	3.0 ± 0.2	3.3 ± 0.2	3.9 ± 0.5	0.85 ± 0.12	Diffuse	Possible
G122.492+2.592	122.492	2.592	10.6	-105.3 ± 0.1	1.4 ± 0.2	1.7 ± 0.3	2.5 ± 0.2	3.5 ± 0.4	0.71 ± 0.10	Diffuse	Possible
G122.775+2.522	122.775	2.522	11.0	-107.2 ± 0.1	2.5 ± 0.1	6.7 ± 0.4	17.9 ± 0.2	12.8 ± 0.6	1.40 ± 0.07	Compact	Possible
G123.367+1.659	123.367	1.659	10.4	-103.0 ± 0.1	2.2 ± 0.1	2.0 ± 0.3	4.5 ± 0.2	6.5 ± 0.5	0.69 ± 0.07	Moderate	With
G123.650+2.833	123.650	2.833	10.7	-104.6 ± 0.1	1.3 ± 0.1	1.8 ± 0.3	2.5 ± 0.2	3.6 ± 0.4	0.69 ± 0.10	Diffuse	Possible
G123.925+3.158	123.925	3.158	10.8	-105.3 ± 0.1	1.2 ± 0.1	2.2 ± 0.3	2.7 ± 0.2	3.2 ± 0.4	0.84 ± 0.13	Diffuse	Possible
G124.292+3.000	124.292	3.000	11.7	-109.8 ± 0.1	1.6 ± 0.2	1.4 ± 0.3	2.4 ± 0.2	3.6 ± 0.5	0.67 ± 0.11	Diffuse	Without
G124.342+3.367	124.342	3.367	10.8	-105.1 ± 0.1	0.9 ± 0.3	1.1 ± 0.3	1.1 ± 0.2	2.8 ± 0.4	0.39 ± 0.10	Diffuse	Without
G124.525+3.400	124.525	3.400	10.6	-104.0 ± 0.1	0.8 ± 0.1	2.1 ± 0.3	1.8 ± 0.1	2.3 ± 0.3	0.78 ± 0.12	Diffuse	Without
G125.075+2.375	125.075	2.375	11.3	-107.4 ± 0.2	1.9 ± 0.3	0.6 ± 0.2	1.3 ± 0.2	3.9 ± 0.5	0.33 ± 0.07	Diffuse	Possible
G127.150+2.583	127.150	2.583	10.6	-101.7 ± 0.1	1.3 ± 0.1	1.4 ± 0.2	1.8 ± 0.2	3.1 ± 0.4	0.58 ± 0.10	Diffuse	Without
G127.875+2.167	127.875	2.167	10.4	-99.5 ± 0.1	1.8 ± 0.2	1.1 ± 0.2	2.1 ± 0.2	4.9 ± 0.5	0.43 ± 0.06	Moderate	With
G128.633+2.833	128.633	2.833	11.1	-102.5 ± 0.1	0.9 ± 0.1	1.2 ± 0.1	1.2 ± 0.1	2.2 ± 0.3	0.55 ± 0.09	Diffuse	Without
G130.050+2.108	130.050	2.108	11.4	-102.5 ± 0.1	1.0 ± 0.1	2.2 ± 0.3	2.2 ± 0.1	3.4 ± 0.4	0.65 ± 0.09	Diffuse	With
G131.016+1.524	131.016	1.524	11.6	-101.8 ± 0.1	2.0 ± 0.1	2.3 ± 0.2	5.0 ± 0.2	7.2 ± 0.5	0.69 ± 0.06	Moderate	With
G131.157+1.390	131.157	1.390	11.3	-100.7 ± 0.1	2.2 ± 0.1	3.3 ± 0.3	7.8 ± 0.2	8.6 ± 0.5	0.91 ± 0.06	Moderate	With
G131.575+1.300	131.575	1.300	12.4	-104.3 ± 0.1	1.6 ± 0.2	1.9 ± 0.2	3.3 ± 0.2	1.6 ± 0.4	2.06 ± 0.54	Moderate	Without
G132.792-0.425	132.792	-0.425	11.0	-97.0 ± 0.1	1.9 ± 0.2	1.4 ± 0.2	2.9 ± 0.2	3.9 ± 0.6	0.74 ± 0.13	Moderate	Without
G133.817-0.758	133.817	-0.758	10.7	-94.6 ± 0.1	1.3 ± 0.1	6.5 ± 0.4	8.8 ± 0.2	5.4 ± 0.3	1.63 ± 0.10	Compact	With
G133.825-0.017	133.825	-0.017	10.0	-90.9 ± 0.1	0.9 ± 0.2	0.7 ± 0.1	0.6 ± 0.2	1.8 ± 0.3	0.33 ± 0.13	Diffuse	Without
G136.859+1.557	136.859	1.557	10.7	-90.9 ± 0.1	1.9 ± 0.2	1.4 ± 0.3	2.8 ± 0.2	3.5 ± 0.5	0.80 ± 0.13	Moderate	Without
G137.283-1.150	137.283	-1.150	14.0	-101.6 ± 0.1	1.5 ± 0.1	3.2 ± 0.2	5.0 ± 0.2	6.9 ± 0.6	0.72 ± 0.07	Moderate	Without
G137.517-1.267	137.517	-1.267	13.1	-98.3 ± 0.1	1.3 ± 0.2	1.6 ± 0.2	2.2 ± 0.2	3.2 ± 0.5	0.69 ± 0.13	Diffuse	Without
G137.617-1.225	137.617	-1.225	13.2	-98.4 ± 0.1	1.9 ± 0.1	3.4 ± 0.2	6.9 ± 0.2	5.6 ± 0.5	1.23 ± 0.12	Compact	With
G137.759-0.983	137.759	-0.983	14.7	-103.1 ± 0.1	2.9 ± 0.1	6.0 ± 0.7	18.7 ± 0.2	17.6 ± 0.5	1.06 ± 0.04	Compact	With
G137.775-1.067	137.775	-1.067	14.4	-102.0 ± 0.1	2.7 ± 0.1	6.2 ± 0.3	17.5 ± 0.3	12.2 ± 0.5	1.43 ± 0.07	Compact	With
G138.373-0.850	138.373	-0.850	12.3	-94.4 ± 0.1	1.1 ± 0.1	2.7 ± 0.3	3.2 ± 0.2	3.2 ± 0.3	1.00 ± 0.12	Moderate	Without
G139.116-1.475	139.116	-1.475	13.4	-96.8 ± 0.1	1.9 ± 0.1	10.2 ± 0.6	20.4 ± 0.2	6.7 ± 0.6	3.04 ± 0.28	Compact	Without
G139.850+0.368	139.850	0.368	11.4	-89.3 ± 0.1	0.7 ± 0.1	1.6 ± 0.1	1.2 ± 0.2	2.9 ± 0.3	0.41 ± 0.09	Diffuse	Without
G140.183+0.258	140.183	0.258	11.4	-88.5 ± 0.1	0.9 ± 0.2	1.1 ± 0.2	1.0 ± 0.2	1.8 ± 0.3	0.56 ± 0.15	Diffuse	Without
G140.700+0.150	140.700	0.150	11.2	-86.9 ± 0.1	1.4 ± 0.2	1.6 ± 0.3	2.5 ± 0.2	2.5 ± 0.5	1.00 ± 0.22	Diffuse	Without
G141.083+0.425	141.083	0.425	11.6	-84.7 ± 0.1	0.9 ± 0.2	1.4 ± 0.2	1.3 ± 0.2	2.6 ± 0.5	0.50 ± 0.13	Diffuse	Without
G142.167+0.267	142.167	0.267	11.8	-85.8 ± 0.2	1.2 ± 0.6	0.6 ± 0.1	0.7 ± 0.3	2.3 ± 0.4	0.30 ± 0.15	Diffuse	Without
G142.642+0.317	142.642	0.317	10.5	-81.3 ± 0.1	1.7 ± 0.3	0.8 ± 0.2	1.4 ± 0.2	2.0 ± 0.3	0.70 ± 0.15	Diffuse	Possible
G143.325+1.775	143.325	1.775	10.4	-79.9 ± 0.1	1.0 ± 0.1	2.4 ± 0.2	2.5 ± 0.2	3.1 ± 0.4	0.81 ± 0.13	Diffuse	With

Notes. Column 1: source name. Columns 2 and 3: Galactic coordinates. Column 4: heliocentric distance taken from [Sun et al. \(2015\)](#). Columns 5–8: results of Gaussian fits to the CO $J=2-1$ spectra. Column 9: integrated intensities of the CO $J=1-0$ spectra taken from [Sun et al. \(2015\)](#). Column 10: the CO $J=2-1/1-0$ integrated intensity ratio. Column 11: classification for the degree of compactness of molecular clouds. Classification by eye, according to velocity-integrated intensity maps of molecular clouds (see Fig. A.1). Column 12: Galactic edge clouds with or without star-forming (SF) activity, which are determined by *WISE*-certified young stars according to [Sun \(2015\)](#).

CO (2–1) transition, the linewidth ranges from 0.7 to 2.9 km s⁻¹, with an average of 1.6 ± 0.2 km s⁻¹. The agreement observed in both CO (1–0) and (2–1) lines indicates that they possibly trace similar components of molecular gas. In these Galactic edge

clouds, R_{21} therefore appears to be a meaningful quantity to be studied.

Table 1. continued.

Sources	l °	b °	d kpc	V_{LSR} km s $^{-1}$	ΔV km s $^{-1}$	T_{mb} K	$I_{\text{CO}(2-1)}$ K km s $^{-1}$	$I_{\text{CO}(1-0)}$ K km s $^{-1}$	R_{21}	Structure	SF Activity
G143.533+0.492	143.533	0.492	9.7	-76.5 ± 0.1	1.4 ± 0.1	3.5 ± 0.3	5.2 ± 0.2	6.5 ± 0.5	0.80 ± 0.07	Compact	With
G144.167+0.817	144.167	0.817	9.4	-74.7 ± 0.1	1.7 ± 0.1	3.1 ± 0.3	5.7 ± 0.2	4.6 ± 0.5	1.24 ± 0.15	Compact	Without
G145.208-0.392	145.208	-0.392	9.7	-73.9 ± 0.1	1.7 ± 0.1	9.2 ± 0.7	16.9 ± 0.2	8.8 ± 0.5	1.92 ± 0.12	Compact	Without
G145.808-1.817	145.808	-1.817	11.6	-79.6 ± 0.1	0.8 ± 0.1	1.8 ± 0.1	1.5 ± 0.2	3.6 ± 0.5	0.42 ± 0.09	Diffuse	Without
G145.850-1.717	145.850	-1.717	11.3	-78.7 ± 0.1	1.4 ± 0.2	1.5 ± 0.2	2.4 ± 0.3	4.4 ± 0.5	0.55 ± 0.10	Diffuse	Without
G146.059-1.650	146.059	-1.650	11.0	-77.3 ± 0.1	1.6 ± 0.1	8.9 ± 0.4	15.3 ± 0.2	8.7 ± 0.4	1.76 ± 0.09	Compact	With

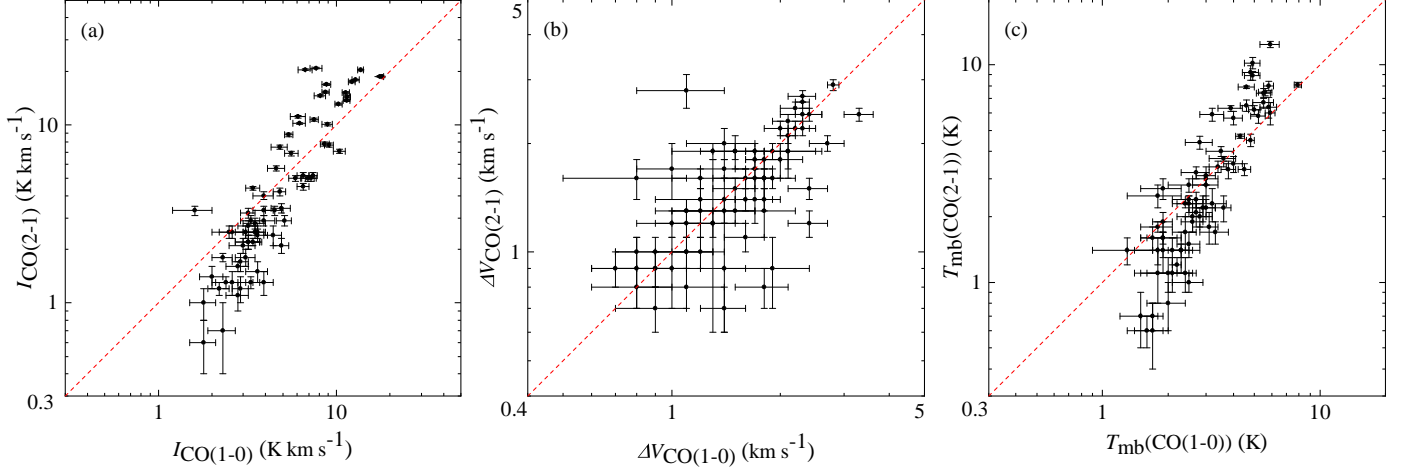


Fig. 3. Correlations of integrated intensities (a), linewidths (b), and peak temperatures (c) of CO(1–0) and (2–1) lines. The red dashed lines indicate $Y = X$.

3.2. R_{21} line ratios

As illustrated in Fig. 2 and Table 1, approximately 40% of the CO(1–0) emissions in these Galactic edge clouds are weaker than CO(2–1). Specifically, the observed range of the R_{21} ratio within the Galactic edge clouds ranges from 0.30 to 3.04, with a mean of 0.97 ± 0.12 and a median of 0.81 ± 0.10 (see Table 1). Our observations show significant variations in the R_{21} ratios by a factor of around five, reaching a full order of magnitude when comparing the lowest with the highest R_{21} value.

The statistical histogram and cumulative distribution of the R_{21} ratio are depicted in Fig. 4. The majority of R_{21} values fall within the range of 0.5–0.9 and there is a systematic prevalence of occurrences for $R_{21} > 0.7$ compared to $R_{21} < 0.7$. Additionally, there exist three sources where R_{21} exceeds 2.0, which are G117.576+3.950, G131.575+1.300, and G139.116–1.475. Such elevated R_{21} ratios stem from the considerably higher peak temperature of CO(2–1) relative to CO(1–0), with the exception of G131.575+1.300, where the linewidth is the primary contributor (see Fig. 2 and discussion in Sect. 4.3.2). Counts of R_{21} values categorized into four distinct groups (see Sect. 1.2) are presented in Table 2. The quantities of the VLRG, LRG, HRG, and VHRG in the 72 Galactic edge clouds are 5, 21, 19, and 27, respectively. Percentages of VLRG, LRG, HRG, and VHRG are 6.9%, 29.2%, 26.4%, and 37.5%, respectively, indicating an increasing trend. These results suggest that the proportion of high R_{21} ratios (≥ 0.7) is significant in molecular clouds at the edge of the Galaxy. Specifically, the mean R_{21} values are as follows: 0.35 ± 0.11 with a corresponding median of 0.33 ± 0.10 , 0.59 ± 0.10 with a median of 0.58 ± 0.10 , 0.80 ± 0.11 with a median of 0.80 ± 0.12 , and 1.51 ± 0.14 with a median of 1.40 ± 0.12 for VLRG, LRG, HRG, and VHRG, respectively (see Table 2). For each of these four R_{21} categories of molecular gas, both mean and median ratios are approximately equivalent.

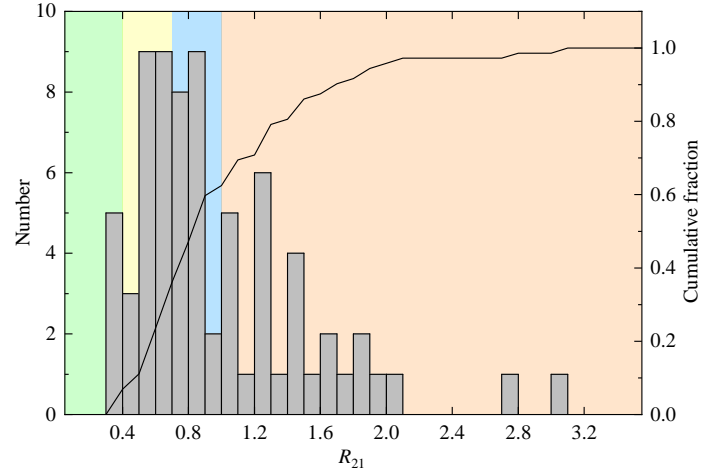


Fig. 4. Histogram of the R_{21} ratios. The solid line shows the cumulative distribution function. The background colors green, yellow, cyan, and orange are used to denote the VLRG, LRG, HRG, and VHRG categories, respectively (see Sect. 1.2).

Table 2. Counts of four R_{21} categories.

Categories	Range	Mean	Median	Counts	Percentage
VLRG	$R_{21} < 0.4$	0.35 ± 0.11	0.33 ± 0.10	5	6.9%
LRG	$0.4 \leq R_{21} < 0.7$	0.59 ± 0.10	0.58 ± 0.10	21	29.2%
HRG	$0.7 \leq R_{21} < 1.0$	0.80 ± 0.11	0.80 ± 0.12	19	26.4%
VHRG	$R_{21} \geq 1.0$	1.51 ± 0.14	1.40 ± 0.12	27	37.5%

3.3. Correlations of R_{21} with CO line parameters

The correlations between the R_{21} ratios and CO line parameters are illustrated in Fig. 5. Positive correlations are observed between the R_{21} ratios and both the CO integrated intensities

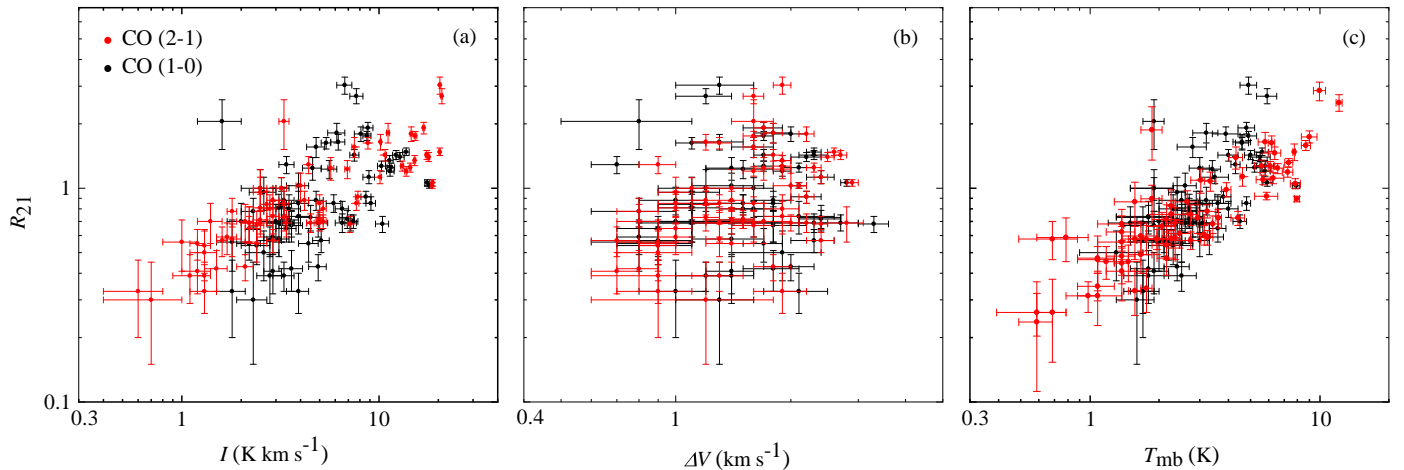


Fig. 5. Correlations between R_{21} and integrated intensities (a), linewidths (b), and peak temperatures (c) of CO lines. Addressed are all our observed 72 Galactic edge clouds. The black and red points denote CO (1–0) and (2–1), respectively.

and peak temperatures. In general, the Galactic edge clouds exhibit higher R_{21} in regions with higher CO intensities. There is a weak correlation between the R_{21} ratios and the linewidths of the CO lines. Furthermore, the linewidth ratio is close to unity (see Sect. 3.1), indicative of uniform linewidths in both CO (1–0) and CO (2–1). Consequently, the CO integrated intensity ratio aligns with the peak temperature ratio, as depicted in Fig. 6.

4. Discussion

4.1. Variation of R_{21} ratios in the Milky Way

The variation of the R_{21} ratio with Galactocentric distance across the entire Galactic disk is depicted in Fig. 7. Within the inner Galaxy, the R_{21} ratio appears to decrease as a function of Galactocentric radius. Notably, the R_{21} ratios decrease from 0.9–1.0 in the central region to ~ 0.7 within the molecular ring of the Milky Way (Chiar et al. 1994; Oka et al. 1998; Sawada et al. 2001). The R_{21} ratio varies from 0.75 ± 0.06 at $R_g = 4$ kpc to 0.6 ± 0.1 in the solar neighborhood (e.g., Handa et al. 1993; Chiar et al. 1994; Handa et al. 1999; Sakamoto et al. 1995, 1997; Hasegawa 1997; Usuda et al. 1999). However, within a range of approximately 8–14 kpc, the R_{21} ratio displays significant variability and does not adhere to this trend. In the inner Galaxy, a mixture of compact components containing high ratio gas and diffuse gas components enveloping these compact structures, characterized by lower ratios, is observed. In contrast, only compact components emitting CO are detected in the outer Galaxy. These results suggest that the relevant R_{21} ratios in the outer Galaxy may be an indication of dense molecular gas poised for significant star formation (Usuda et al. 1999). These measurements of R_{21} are consistent with those obtained from the Galactic edge clouds, suggesting that the physical conditions within these molecular clouds may be analogous in both the outer Galaxy and the Galactic edge clouds.

4.2. R_{21} in external galaxies

4.2.1. Magellanic Clouds

The metallicity of the Galactic edge clouds exhibits similarities to metal-poor galaxies such as the LMC and SMC (Yasui et al. 2006, 2008). The R_{21} ratios in the Galactic edge clouds (see Sect. 3.2) show a broader distribution than those in the LMC

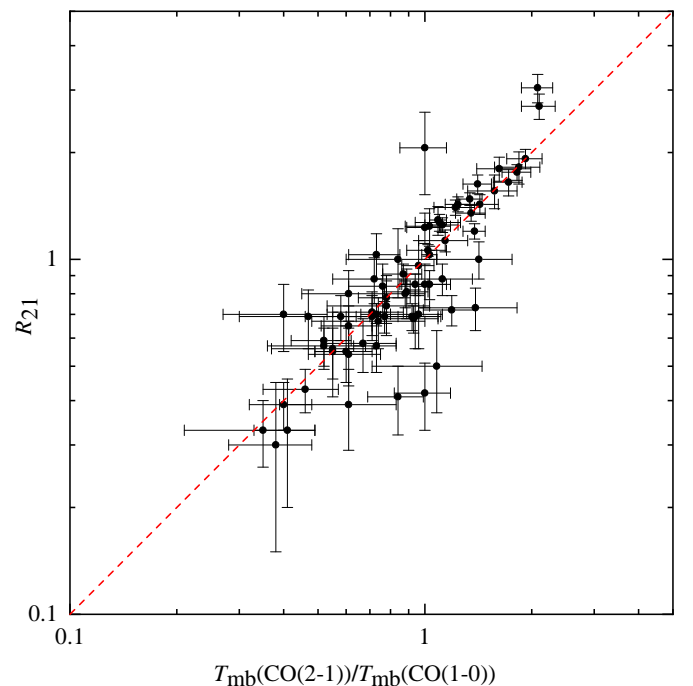


Fig. 6. Correlation between R_{21} ratios and CO brightness temperature ratios. The red dashed line indicates $Y = X$.

(0.5–>1.3; Heikkilä et al. 1999; Bolatto et al. 2000; Sorai et al. 2001), likely due to a larger number of observed samples and higher linear resolution. The average R_{21} value of 0.92 ± 0.05 in the LMC (Sorai et al. 2001) is similar to the mean R_{21} in the Galactic edge clouds. The R_{21} ratio within 30 Doradus cloud complex is 0.95 ± 0.06 , consistent with our average results in the Galactic edge clouds but higher than those observed in the outer regions of the LMC. The maximum R_{21} value of 3.04 in the Galactic edge clouds is consistent with an extended envelope with $R_{21} > 3$ in the N159/N160 complex of the LMC (Bolatto et al. 2000). Subsequently, the presence of the VHRG with R_{21} values exceeding 2.0 has been discovered within the N83/N84 molecular cloud complex of the SMC. The typical value of R_{21} is around 1.0 in the molecular clouds of the SMC (Heikkilä et al. 1999; Bolatto et al. 2003), which is also consistent with our mean R_{21} observed in the Galactic edge clouds. The simi-

lar mean values of R_{21} observed in the Galactic edge clouds, the LMC, and the SMC indicate that the physical conditions within these molecular clouds may be comparable.

In the LMC, a radial gradient in the R_{21} ratio is observed at distances from the center out to ~ 4 kpc, with the ratio measuring 0.94 ± 0.34 in the inner region ($\lesssim 2$ kpc from the kinematic center) and 0.69 ± 0.27 in the outer region ($\gtrsim 2$ kpc from the center, excluding the 30 Doradus complex) (Sorai et al. 2001). This indicates that the inner clouds are both warmer ($T_{\text{kin}} > 20\text{--}40$ K) and/or denser ($n_{\text{H}_2} > 10^3 \text{ cm}^{-3}$) than the outer clouds of the LMC. The radial variation observed in the inner Galaxy exhibits a similar trend to that observed in the LMC, which may indicate a shared mechanism that dictates the average physical conditions of molecular gas on large scales within disk galaxies, despite their morphological differences (Sorai et al. 2001). However, the mean R_{21} ratio in the Galactic edge clouds is higher compared to the outer region of the LMC, indicating potential differences in the physical conditions of molecular clouds between the edge of our Galaxy and the outer region of the LMC.

4.2.2. Other nearby galaxies

The investigation of the R_{21} ratio has been conducted on a significant number of extragalactic sources located beyond the Magellanic Clouds. Analogous to the Milky Way and Magellanic Clouds, the R_{21} ratio exhibits a variation ranging from approximately 0.3 to 2.6, as established through CO multi-line surveys of external galaxies (e.g., Braine & Combes 1992; Leroy et al. 2009; Papadopoulos et al. 2012; Leroy et al. 2013, 2022; Israel 2020; den Brok et al. 2021; Yajima et al. 2021; Keenan et al. 2024). Similar to the situation in the Milky Way, the Galactic R_{21} ratio displays a slight trend of an initial radial decline followed by a higher dispersion in the nearby barred spiral galaxy NGC 2903 (den Brok et al. 2021). In NGC 2903, high star formation efficiency concentrates in central zones and H II regions distributed along its bar (Alonso-Herrero et al. 2001; Popping et al. 2010). Notably, the central regions of many of these galaxies display consistently elevated R_{21} ratios (e.g., Braine & Combes 1992; Leroy et al. 2009, 2013; Israel 2020; den Brok et al. 2021; Yajima et al. 2021). The R_{21} dispersion increases with distance from the center, both for our Galaxy and nearby galaxies (see also Fig. 7 and Fig. 3 in den Brok et al. 2021).

In addition to the Milky Way, CO gas has been detected extending beyond the nominal R_{25} radius⁷ in a few galaxies, including NGC 4414 (~ 13 kpc), M 33 (~ 9 kpc), M 51 ($R_{25} \sim 12$ kpc) and M 83 ($R_{25} \sim 18$ kpc) (e.g., Braine et al. 1993b; Braine & Herpin 2004; Koda et al. 2012, 2020; Druard et al. 2014). A variable R_{21} ratio has also been observed in the outer disks of some nearby galaxies. Specifically, the R_{21} ratio is measured to be $\lesssim 0.5$ at the optical edge of NGC 4414 (Braine & Herpin 2004), and this ratio does not exhibit dependence on galactocentric distance (Braine et al. 1993b). Furthermore, the R_{21} ratio in the outer disk of M 33 is ~ 0.8 , showing no significant variation with galactocentric radius (Druard et al. 2014). The R_{21} ratio demonstrates an increase towards the downstream side of the spiral arms, subsequently decreasing to 0.60 in the outer regions of M 51 and M 83 (Koda et al. 2012, 2020). Possibly as a consequence of the larger applied beam sizes, the R_{21} ratios in the outer disks of nearby galaxies seem to be influenced by larger scale factors than our Galactic edge clouds.

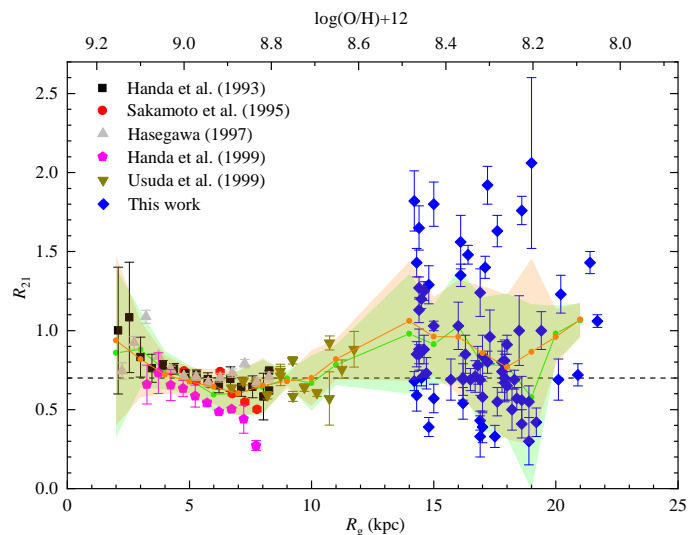


Fig. 7. Variation of the R_{21} ratios with Galactocentric distance R_g . The orange values refer to 1 kpc bins with orange straight lines connecting them (unweighted mean value within a bin), and dispersion indicating the propagated uncertainty. The green values, weighted by the square of the uncertainties, correspond to 1 kpc bins. Values of $R_{21} > 2.2$ are not shown here and values of $R_g < 14$ kpc are obtained from previous measurements (Handa et al. 1993, 1999; Sakamoto et al. 1995; Hasegawa 1997; Usuda et al. 1999). The black horizontal dotted line denotes a value of $R_{21} = 0.7$.

4.3. Enhancement of R_{21}

The R_{21} ratio can serve as a tracer of gas-compressed regions characterized by relatively high temperatures and densities (e.g., Vaduvescu et al. 2007; Zhang et al. 2019). Radiative transfer solutions of CO lines are detailed in Appendix B. The R_{21} ratio ($R_{21} \sim T_{\text{mb}}(2-1)/T_{\text{mb}}(1-0)$; see Sect. 3.3 or Fig. 6) converges towards unity under conditions of optically thick, warm, and dense gas assuming LTE. In scenarios of optically thin emission, the R_{21} ratio could potentially reach up to values of four in dense and warm gas. Empirical evidence suggests that regions with high R_{21} ratios are commonly associated with dense cloud and/or active star-forming regions.

4.3.1. Star-forming activity

Previous studies have probed high R_{21} ratios as caused by massive star formation activity. GMCs that exhibit active star formation tend to have higher R_{21} ratios, whereas those with quiescent star formation display lower ratios (Sakamoto et al. 1994; Nishimura et al. 2015; Yajima et al. 2021; Egusa et al. 2022). Star formation activity has been identified within Digel Cloud 1 and 2 (see Sec. 2.1). Two sources we observed, G131.016+1.524 and G131.157+1.390, located within Digel Cloud 1, are classified as moderate clouds (see Sect. 3.1) and are associated with star-formation activity (see Table 1). Additionally, G137.759–0.983 and G137.775–1.067 situated within Digel Cloud 2, are compact clouds that exhibit a correlation with star-formation activity. The molecular gas within the Digel Cloud is characterized by notably high R_{21} ratios (0.69–1.43). It is more likely for molecular gas to exhibit characteristics of being warm, dense, and optically thin when $R_{21} > 2.0$ (for G117.576+3.950, G131.575+1.300, and G139.116–1.475). Nevertheless, two of the three sources are not associated with star-formation activity. The exception is G117.576+3.950. The highest R_{21} value,

⁷ R_{25} radius was taken from the NASA/IPAC Extragalactic Database (NED).

Table 3. The typical linewidth and brightness temperature of CO lines in different R_{21} classifications

Categories	CO (1–0)				CO (2–1)			
	ΔV (km s ⁻¹)		T_{mb} (K)		ΔV (km s ⁻¹)		T_{mb} (K)	
	Mean	Median	Mean	Median	Mean	Median	Mean	Median
VLRG	1.4 ± 0.3	1.3 ± 0.2	1.9 ± 0.4	1.7 ± 0.3	1.2 ± 0.4	1.2 ± 0.3	0.8 ± 0.2	0.7 ± 0.1
LRG	1.6 ± 0.3	1.6 ± 0.3	2.4 ± 0.8	2.3 ± 0.4	1.4 ± 0.2	1.3 ± 0.1	1.6 ± 0.2	1.6 ± 0.2
HRG	1.5 ± 0.3	1.5 ± 0.2	2.9 ± 0.4	2.7 ± 0.4	1.4 ± 0.2	1.4 ± 0.1	2.6 ± 0.3	2.4 ± 0.2
VHRG	1.7 ± 0.2	1.7 ± 0.2	4.4 ± 0.4	4.6 ± 0.4	1.9 ± 0.2	1.8 ± 0.1	6.0 ± 0.4	6.2 ± 0.3
Diffuse	1.3 ± 0.3	1.2 ± 0.2	2.2 ± 0.4	2.0 ± 0.3	1.3 ± 0.2	1.2 ± 0.2	1.5 ± 0.3	1.5 ± 0.2
Moderate	1.7 ± 0.3	1.6 ± 0.2	2.8 ± 0.4	2.6 ± 0.4	1.5 ± 0.2	1.5 ± 0.1	2.4 ± 0.3	2.3 ± 0.2
Compact	1.7 ± 0.2	1.7 ± 0.2	4.7 ± 0.4	4.8 ± 0.4	1.9 ± 0.1	1.9 ± 0.1	6.4 ± 0.4	6.3 ± 0.4
Without SF	1.4 ± 0.3	1.4 ± 0.2	2.4 ± 0.4	2.3 ± 0.4	1.3 ± 0.2	1.3 ± 0.1	2.4 ± 0.3	1.7 ± 0.2
Possible SF	1.5 ± 0.3	1.4 ± 0.2	3.3 ± 0.4	3.0 ± 0.4	1.7 ± 0.2	1.6 ± 0.1	2.7 ± 0.3	2.2 ± 0.3
With SF	1.9 ± 0.2	1.9 ± 0.2	4.2 ± 0.4	4.0 ± 0.4	1.8 ± 0.1	1.9 ± 0.1	5.2 ± 0.3	5.8 ± 0.3

Notes. The classifications are described in Tables 1 and 2.

measured at 3.04, is observed in G139.116–1.475. This object is characterized by its compact structure and lack of star formation activity. The absence of notable star formation activity in G139.116–1.475 may hint at external heating by neighboring stars or it may be a sign of an extremely early phase in the star formation process.

We conduct a statistical analysis to explore the correlation between the R_{21} ratio of Galactic edge clouds and their association with star-forming activity in Figs. 8 and 9. Based on the association between molecular clouds and star formation activity with the *WISE*-certified young stars (for details, see Sun 2015), 72 Galactic edge clouds were systematically classified into three distinct categories: with star formation, possible star formation, and without star formation (see Table 1). This evaluation demonstrates that the HRG and VHRG molecular clouds are closely linked to star formation, as well as possible star formation (see Fig. 8). Star formation activity is notably weak in the VLRG molecular clouds. Within Galactic edge clouds associated with star formation activity, the proportion of VHRG to the total molecular gas surpasses that in the clouds without star formation activity. It seems that Galactic edge clouds, which exhibit star formation activity, typically display higher R_{21} ratios compared to those clouds devoid of such activity. In addition, only those relatively large and massive clouds may be detected at such distances. So a high R_{21} is not unexpected.

Previous observations suggest that the R_{21} ratio exhibits a positive correlation with star formation rate indicators, including H α emission (pc scale) (e.g., Egusa et al. 2022; Maeda et al. 2022), the surface density of star-formation rate (kpc scale) (e.g., Yajima et al. 2021; Leroy et al. 2022; Maeda et al. 2023; Jiang et al. 2024; Keenan et al. 2025), and infrared emission (kpc scale) (e.g., Braine & Combes 1992; Koda et al. 2012, 2020; Yajima et al. 2021; den Brok et al. 2021). This suggests that the relatively high R_{21} ratio in the Galactic edge clouds may be considered on smaller scales with star-forming clouds, as well as on larger scales with star-forming galaxies. However, we did not find any evidence to suggest that the R_{21} ratios are correlated with infrared flux (*WISE* 3.4–22 μm and *AKARI* 65–160 μm , see Fig. 10). In addition, R_{21} depends on the gas kinetic temperature, while the infrared luminosity is connected to the dust temperature. This suggests that there is not a close correlation between the kinetic temperature and the dust temperature, due to low gas densities. The R_{21} ratios are not significantly linked to metallicity gradients with Galactocentric distance in the outer Galaxy (see Sect. 4.1 or Fig. 7). The variable R_{21} values appear to corre-

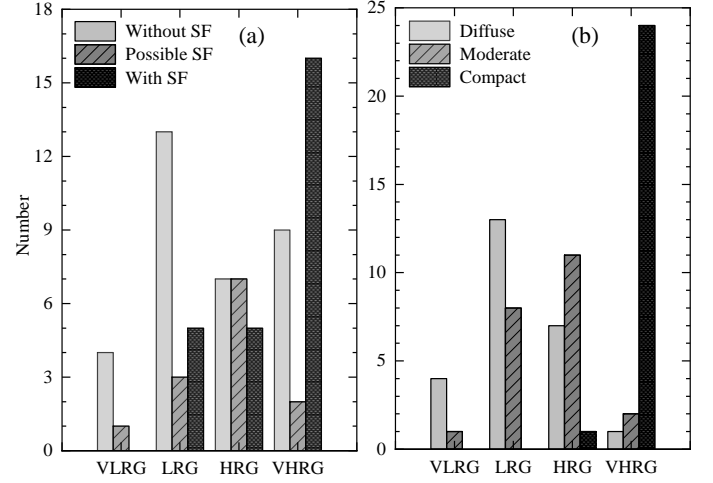


Fig. 8. Histograms connecting R_{21} (a) with the star formation properties and (b) with the compactness of our 72 targets. For the classification of VLRG, LRG, HRG, and VHRG clouds, see Sect. 1.2. For the determination of star-forming activity, see Sect. 4.3.1, while Sect. 4.3.2 refers to the overall structure of the clouds.

spond to molecular clouds at different evolutionary stages of the star-forming process at the edge of the Galaxy.

4.3.2. Clumpy structure

In low-metallicity environments, diffuse areas within molecular clouds may lack sufficient dust to protect CO molecules from photodissociation. Observations have shown high R_{21} ratio gas with compact components, as well as low ratio gas with diffuse components (e.g., Sakamoto et al. 1994; Usuda et al. 1999; Hasegawa 1997; Sorai et al. 2001; Nishimura et al. 2015). The R_{21} ratios of our Galactic edge clouds were statistically examined by categorizing the compactness levels of molecular clouds (diffuse, moderate, and compact; see Sect. 3.1) in Figs. 8 and 9. The compact clouds tend to exhibit higher R_{21} ratios than the diffuse and moderate clouds. Previous observations indicate that the fraction of CO-dark H₂ to total H₂ increases with Galactocentric distance, ranging from ~20% at 4 kpc to ~80% at 10 kpc (Pineda et al. 2013). In the solar neighborhood, approximately half of the molecular gas is CO-dark (e.g., Paradis et al. 2012; Pineda et al. 2013; Chen et al. 2015). This contribution should be even more significant in the low metallicity regions of the Galac-

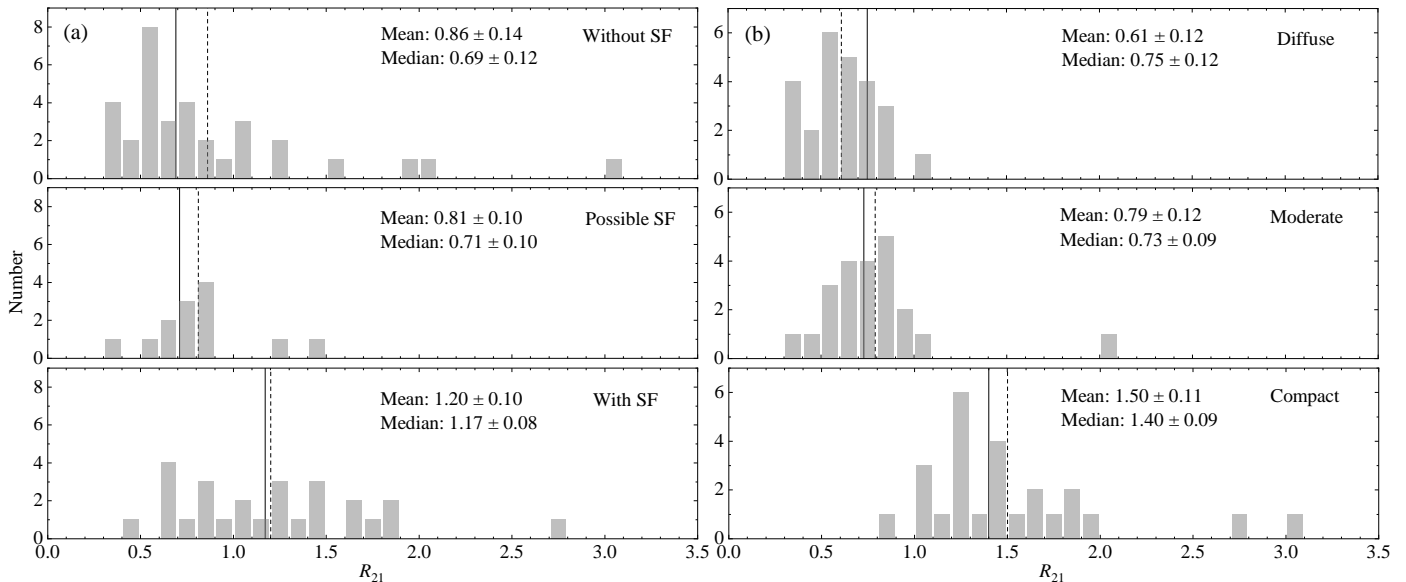


Fig. 9. Histograms connecting R_{21} (a) with the star formation properties and (b) with the compactness of our 72 targets. For the classification of VLRG, LRG, HRG, and VHRG clouds, see Sect. 1.2. For the determination of star-forming activity, see Sect. 4.3.1, while Sect. 4.3.2 refers to the overall structure of the clouds. The dotted lines and the solid lines denote the mean and the median values, respectively.

tic edge clouds (Pineda et al. 2013; Langer et al. 2014; Luo et al. 2024). As a result, only regions with particularly high column density are seen in CO emissions, thereby enhancing the R_{21} ratio.

4.3.3. Linewidths, compactness, and brightness temperatures

Regardless of CO (1–0) or (2–1), both the mean and median linewidths demonstrate a progressive increase, ranging from VLRG to VHRG (see Table 3). Similarly, average CO linewidth values are higher in compact clouds compared to those in diffuse clouds. Furthermore, the linewidths are broader in the Galactic edge clouds that exhibit star formation compared to those devoid of such activity (see Table 3). Nevertheless, the CO linewidths of our Galactic edge clouds are systematically narrow with a mean value of $\sim 1.6 \text{ km s}^{-1}$ (see Sect. 3.1 and Table 1). This is similar to observational results from CO in infrared dark clouds (e.g., Li et al. 2016) but much smaller than typical values ($\sim \text{few km s}^{-1}$) observed with multiple molecular species in massive star-forming regions of our Galaxy and the LMC (e.g., Tang et al. 2013, 2014, 2017a,b, 2018a,b, 2021; Giannetti et al. 2014, 2017; Gong et al. 2023; Green et al. 2024; Zhao et al. 2024). The brightness temperature of CO lines exhibits an increase from diffuse to compact clouds within the Galactic edge clouds. This trend is also observed in the transition from low- to high-ratio gas of R_{21} (see Table 3). It may imply that the majority of high R_{21} clouds in the extreme outer Galaxy are more likely to form stars due to their intrinsic density, rather than due to external pressure.

4.3.4. Galactic arm

The radial variation of R_{21} may be caused by the mixing ratio variation of molecular gas with different R_g (Sakamoto et al. 1997). The R_{21} ratio increases from < 0.7 in the interarm regions to > 0.7 in the spiral arms (e.g., Koda et al. 2012, 2020; Maeda et al. 2022), indicating a substantial fraction of the high R_{21} gas in the spiral arms and a larger fraction of the low R_{21} gas in

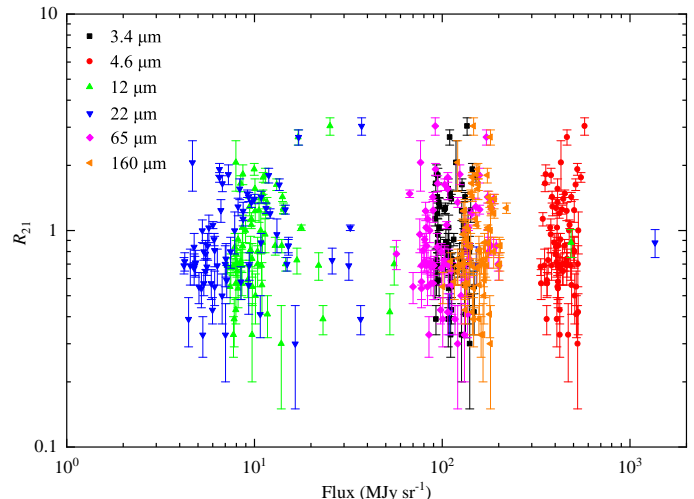


Fig. 10. No correlation between R_{21} ratios and infrared flux.

the interarm regions. The Galactic edge clouds we observed are situated on a new arm (see Sect. 1.1), and the enhancements of the R_{21} ratio on scales of 2.3–3.7 pc are attributed to this region. Considering these factors, it appears that the R_{21} radial trend in the Galaxy is likely due to arm-like structures and/or mixing ratios of multiple R_{21} gases. However, variation of R_{21} in the Galactic edge clouds is likely caused by multi-scale and multi-physical processes, and a simple explanation is not entirely convincing. Therefore, further studies involving more samples and diverse molecular probes are anticipated for the investigation of Galactic edge clouds.

5. Summary

We conducted observations of CO ($J=2-1$) spectral lines towards 72 molecular clouds in the Galactic edge at Galactocentric distances of $R_g = 14-22 \text{ kpc}$, utilizing the IRAM 30 m telescope. By integrating the CO ($J=1-0$) data obtained from the MWISP

project, we investigated the variations of the R_{21} ratios across these Galactic edge clouds. The main results are the following:

1. CO(2–1) has been detected in all observed 72 sources. With a resolution of $52''$ and accounting for beam size effects, the R_{21} ratio values derived from CO(2–1) to (1–0) integrated intensity ratios span from 0.30 to 3.04 with a mean of 0.97 ± 0.12 and a median of 0.81 ± 0.10 in 72 Galactic edge clouds. The proportions of VLRG, LRG, HRG, and VHRG (see Sect. 1.2) are found to be 6.9%, 29.2%, 26.4%, and 37.5%, respectively. This indicates a significant presence of molecular gas with a high proportion and elevated excitation levels within the Galactic edge clouds.
2. The R_{21} ratio in our Galaxy shows a gradient of initial radial decline followed by a high dispersion in Galactocentric distance, akin to that observed in NGC 2903. The scattering R_{21} ratio does not display a systematic variation within the range of $R_g = 14$ –22 kpc at the periphery of the Milky Way.
3. The high proportion of HRG and VHRG in our edge clouds is correlated with compact clouds and regions exhibiting star-forming activity. This implies that the high R_{21} ratios could be attributed to dense gas concentrations and recent episodes of star formation.

The Galactic edge clouds present an ideal location for investigating molecular clouds and star formation within low metallic environments. Future research will focus on the comprehensive investigation of the physical and chemical characteristics of the Galactic edge clouds.

Acknowledgements. The authors thank the referee for helpful comments. We thank the staff of the IRAM telescope for their assistance in observations. This work acknowledges the support of the National Key R&D Program of China under grant Nos. 2023YFA1608002 and 2022YFA1603103, the Tianshan Talent Training Program of Xinjiang Uygur Autonomous Region under grant No. 2022TSYCLJ0005, the Chinese Academy of Sciences (CAS) “Light of West China” Program under grant No. xzbzg-zdsys-202212, and the Natural Science Foundation of Xinjiang Uygur Autonomous Region under grant No. 2022D01E06. It was also partially supported by the Regional Collaborative Innovation Project of Xinjiang Uygur Autonomous Region under grant No. 2022E01050, the National Natural Science Foundation of China under grant Nos. 12173075, 12373029, and 12463006, the Xinjiang Key Laboratory of Radio Astrophysics under grant No. 2023D04033, the Natural Science Foundation of Xinjiang Uygur Autonomous Region under grant No. 2022D01A359, and the Youth Innovation Promotion Association CAS. C. Henkel acknowledges support by the Chinese Academy of Sciences President’s International Fellowship Initiative under grant No. 2025PVA0048. X. P. Chen, T. Liu, K. Wang, and J. W. Wu acknowledge support by the Tianchi Talent Program of Xinjiang Uygur Autonomous Region. MWISP is sponsored by the National Key R&D Program of China with grant 2023YFA1608000 and the CAS Key Research Program of Frontier Sciences with grant QYZDJ-SSW-SLH047. This research has used NASA’s Astrophysical Data System (ADS).

References

Alonso-Herrero, A., Ryder, S. D., & Knapen, J. H. 2001, *MNRAS*, 322, 757
 Arimoto, N., Sofue, Y., & Tsujimoto, T. 1996, *PASJ*, 48, 275
 Armentrout, W. P., Anderson, L. D., Balser, D. S., et al. 2017, *ApJ*, 841, 121
 Bernal, J. J., Sephus, C. D., & Zdziarski, L. M. 2021, *ApJ*, 922, 106
 Blair, S. K., Magnani, L., Brand, J., & Wouterloot, J. G. A. 2008, *Astrophysics*, 8, 59
 Bloemen, J. B. G. M., Deul, E. R., & Thaddeus, P. 1990, *A&A*, 233, 437
 Bolatto, A. D., Jackson, J. M., Israel, F. P., Zhang, X., & Kim, S. 2000, *ApJ*, 545, 234
 Bolatto, A. D., Leroy, A., Israel, F. P., & Jackson, J. M. 2003, *ApJ*, 595, 167
 Bolatto, A. D., Wolfire, M., & Leroy, A. K. 2013, *ARA&A*, 51, 207
 Braine, J. 2017, in *IAU Symposium*, Vol. 321, Formation and Evolution of Galaxy Outskirts, ed. A. Gil de Paz, J. H. Knapen, & J. C. Lee, 217–219
 Braine, J. & Combes, F. 1992, *A&A*, 264, 433
 Braine, J., Combes, F., Casoli, F., et al. 1993a, *A&AS*, 97, 887
 Braine, J., Combes, F., & van Driel, W. 1993b, *A&A*, 280, 451

Braine, J., Ferguson, A. M. N., Bertoldi, F., & Wilson, C. D. 2007, *ApJ*, 669, L73
 Braine, J. & Herpin, F. 2004, *Nature*, 432, 369
 Braine, J., Sun, Y., Shimajiri, Y., et al. 2023, *A&A*, 676, A27
 Brand, J. & Wouterloot, J. G. A. 1994, *A&AS*, 103, 503
 Brand, J. & Wouterloot, J. G. A. 1995, *A&A*, 303, 851
 Brand, J. & Wouterloot, J. G. A. 2007, *A&A*, 464, 909
 Brunt, C. M., Kerton, C. R., & Pomerleau, C. 2003, *ApJS*, 144, 47
 Carilli, C. L. & Walter, F. 2013, *ARA&A*, 51, 105
 Casoli, F., Dupraz, C., Combes, F., & Kazes, I. 1991, *A&A*, 251, 1
 Castets, A., Duvert, G., Dutrey, A., et al. 1990, *A&A*, 234, 469
 Chen, B. Q., Liu, X. W., Yuan, H. B., Huang, Y., & Xiang, M. S. 2015, *MNRAS*, 448, 2187
 Chiar, J. E., Kutner, M. L., Verter, F., & Leous, J. 1994, *ApJ*, 431, 658
 Crosthwaite, L. P. & Turner, J. L. 2007, *AJ*, 134, 1827
 Daddi, E., Dannerbauer, H., Elbaz, D., et al. 2008, *ApJ*, 673, L21
 Dahlem, M., Golla, G., Whiteoak, J. B., et al. 1993, *A&A*, 270, 29
 Dame, T. M., Elmegreen, B. G., Cohen, R. S., & Thaddeus, P. 1986, *ApJ*, 305, 892
 Dame, T. M., Hartmann, D., & Thaddeus, P. 2001, *ApJ*, 547, 792
 Dame, T. M. & Thaddeus, P. 2011, *ApJ*, 734, L24
 Deharveng, L., Schuller, F., Anderson, L. D., et al. 2010, *A&A*, 523, A6
 den Brok, J. S., Bigiel, F., Sliwa, K., et al. 2022, *A&A*, 662, A89
 den Brok, J. S., Chatzigiannakis, D., Bigiel, F., et al. 2021, *MNRAS*, 504, 3221
 Dickman, R. L. 1975, *ApJ*, 202, 50
 Digel, S., de Geus, E., & Thaddeus, P. 1994, *ApJ*, 422, 92
 Doane, N. E., Sanders, W. T., Wilcots, E. M., & Juda, M. 2004, *AJ*, 128, 2712
 Druard, C., Braine, J., Schuster, K. F., et al. 2014, *A&A*, A118
 Eckart, A., Downes, D., Genzel, R., et al. 1990, *ApJ*, 348, 434
 Egusa, F., Gao, Y., Morokuma-Matsui, K., Liu, G., & Maeda, F. 2022, *ApJ*, 935, 64
 Elmegreen, B. G., Rubio, M., Hunter, D. A., et al. 2013, *Nature*, 495, 487
 Enokiya, R., Sano, H., Hayashi, K., et al. 2018, *PASJ*, 70, S49
 Frerking, M. A., Langer, W. D., & Wilson, R. W. 1982, *ApJ*, 262, 590
 Giannetti, A., Leurini, S., König, C., et al. 2017, *A&A*, 606, L12
 Giannetti, A., Wyrowski, F., Brand, J., et al. 2014, *A&A*, 570, A65
 Glover, S. C. O. & Clark, P. C. 2016, *MNRAS*, 456, 3596
 Goldsmith, P. F., Young, J. S., & Langer, W. D. 1983, *ApJS*, 51, 203
 Gong, Y., Henkel, C., Menten, K. M., et al. 2023, *A&A*, 679, L6
 Green, A., Wong, T., Indebetouw, R., et al. 2024, *ApJ*, 966, 51
 Greve, A., Panis, J. F., & Thum, C. 1996, *A&AS*, 115, 379
 Güver, T. & Özel, F. 2009, *MNRAS*, 400, 2050
 Handa, T., Hasegawa, T., Hayashi, M., et al. 1993, in *American Institute of Physics Conference Series*, Vol. 278, Back to the Galaxy, ed. S. S. Holt & F. Verter (AIP), 315–318
 Handa, T., Hasegawa, T., Morino, J. I., et al. 1999, in *Astronomical Society of the Pacific Conference Series*, Vol. 168, New Perspectives on the Interstellar Medium, ed. A. R. Taylor, T. L. Landecker, & G. Joncas, 399
 Hasegawa, T. 1997, *IAU Symposium*, 170, 39
 Hasegawa, T., Morino, J., Sorai, K., et al. 1997, in *Astronomical Society of the Pacific Conference Series*, Vol. 124, Diffuse Infrared Radiation and the IRTS, ed. H. Okuda, T. Matsumoto, & T. Rollig, 244
 Heikkilä, A., Johansson, L. E. B., & Olofsson, H. 1999, *A&A*, 344, 817
 Henkel, C., Hunt, L. K., & Izotov, Y. I. 2022, *Galaxies*, 10, 11
 Henkel, C., Mühle, S., Bendo, G., et al. 2018, *A&A*, 615, A155
 Henkel, C., Wouterloot, J. G. A., & Bally, J. 1986, *A&A*, 155, 193
 Henshaw, J. D., Barnes, A. T., Battersby, C., et al. 2023, in *Astronomical Society of the Pacific Conference Series*, Vol. 534, Protostars and Planets VII, ed. S. Inutsuka, Y. Aikawa, T. Muto, K. Tomida, & M. Tamura, 83
 Herbert-Fort, S., Zaritsky, D., Moustakas, J., et al. 2009, *ApJ*, 700, 1977
 Heyer, M. & Dame, T. M. 2015, *ARA&A*, 53, 583
 Heyer, M., Krawczyk, C., Duval, J., & Jackson, J. M. 2009, *ApJ*, 699, 1092
 Heyer, M. H., Brunt, C., Snell, R. L., et al. 1998, *ApJS*, 115, 241
 Heyer, M. H., Carpenter, J. M., & Snell, R. L. 2001, *ApJ*, 551, 852
 Hunt, L. K., Weiß, A., Henkel, C., et al. 2017, *A&A*, 606, A99
 Indebetouw, R., Wong, T., Madden, S., et al. 2024, *ApJ*, 969, 143
 Iodice, E., Arnaboldi, M., Rejkuba, M., et al. 2014, *A&A*, 567, A86
 Israel, F. P. 2005, *A&A*, 438, 855–866
 Israel, F. P. 2020, *A&A*, 635, A131
 Izumi, N., Kobayashi, N., Yasui, C., Saito, M., & Hamano, S. 2017, *AJ*, 154, 163
 Izumi, N., Kobayashi, N., Yasui, C., et al. 2022, *ApJ*, 936, 181
 Izumi, N., Kobayashi, N., Yasui, C., et al. 2014, *ApJ*, 795, 66
 Izumi, N., Ressler, M. E., Lau, R. M., et al. 2024, *AJ*, 168, 68
 Jiang, Y., Li, J.-T., Gao, Y., et al. 2024, *MNRAS*, 528, 4160
 Jorgenson, R. A., Murphy, M. T., & Thompson, R. 2013, *MNRAS*, 435, 482
 Keenan, R. P., Marrone, D. P., & Keating, G. K. 2025, *ApJ*, 979, 228
 Keenan, R. P., Marrone, D. P., Keating, G. K., et al. 2024, *ApJ*, 975, 150
 Kobayashi, N., Yasui, C., Tokunaga, A. T., & Saito, M. 2008, *ApJ*, 683, 178
 Koda, J., Sawada, T., Sakamoto, K., et al. 2020, *ApJ*, 890, L10
 Koda, J., Scoville, N., Hasegawa, T., et al. 2012, *ApJ*, 761, 41

- Koelemay, L. A., Gold, K. R., & Ziurys, L. M. 2023, *Nature*, 623, 292
- König, C., Urquhart, J. S., Wyrowski, F., Colombo, D., & Menten, K. M. 2021, *A&A*, 645, A113
- Lamperti, I., Saintonge, A., Koss, M., et al. 2020, *ApJ*, 889, 103
- Langer, W. D., Velusamy, T., Pineda, J. L., Willacy, K., & Goldsmith, P. F. 2014, *A&A*, 561, A122
- Leroy, A. K., Rosolowsky, E., Usero, A., et al. 2022, *ApJ*, 927, 149
- Leroy, A. K., Walter, F., Bigiel, F., et al. 2009, *AJ*, 137, 4670
- Leroy, A. K., Walter, F., Sandstrom, K., et al. 2013, *AJ*, 146, 19
- Li, D., Esimbek, J., Zhou, J., et al. 2016, *Ap&SS*, 361, 220
- Li, Z., Li, Z., Smith, M. W. L., et al. 2020, *MNRAS*, 492, 195
- Li, Z.-Q., Zhang, X.-G., Xu, Y., et al. 2021, *Chinese Astron. Astrophys.*, 45, 559
- Lian, J., Bergemann, M., Pillepich, A., Zasowski, G., & Lane, R. R. 2023, *Nature Astronomy*, 7, 951
- Lin, L., Zhang, Z.-Y., Wang, J., et al. 2025, *Nature Astronomy*, 9, 406
- Lindt-Krieg, E., Eckart, A., Neri, R., et al. 2008, *A&A*, 479, 377
- Liu, D., Schinnerer, E., Cao, Y., et al. 2023, *ApJ*, 944, L19
- Loiseau, N., Nakai, N., Sofue, Y., et al. 1990, *A&A*, 228, 331
- Lu, X., Liu, J., Pillai, T., et al. 2024, *ApJ*, 962, 39
- Luo, G., Li, D., Zhang, Z.-Y., et al. 2024, *A&A*, 685, L12
- Ma, Y., Wang, H., Li, C., et al. 2021, *ApJS*, 254, 3
- Maeda, F., Egusa, F., Ohta, K., Fujimoto, Y., & Habe, A. 2023, *ApJ*, 943, 7
- Maeda, F., Egusa, F., Ohta, K., et al. 2022, *ApJ*, 926, 96
- Mangum, J. G. & Shirley, Y. L. 2015, *PASP*, 127, 266
- Mao, R.-Q., Schulz, A., Henkel, C., et al. 2010, *ApJ*, 724, 1336
- Martig, M., Minchev, I., Ness, M., Fouesneau, M., & Rix, H.-W. 2016, *ApJ*, 831, 139
- Matsuo, M., Nakanishi, H., Minamidani, T., et al. 2017, *PASJ*, 69, L3
- Matsuoka, Y., Yuan, F.-T., Takeuchi, Y., & Yanagisawa, K. 2012, *PASJ*, 64, 44
- Mauersberger, R., Henkel, C., Walsh, W., & Schulz, A. 1999, *A&A*, 341, 256
- Mead, K. N. & Kutner, M. L. 1988, *ApJ*, 330, 399
- Miura, R. E., Kohno, K., Tosaki, T., et al. 2014, *ApJ*, 788, 167
- Montoya Arroyave, I., Ciccone, C., Makroleivadioti, E., et al. 2023, *A&A*, 673, A13
- Muraoka, K., Homma, A., Onishi, T., et al. 2017, *ApJ*, 844, 98
- Muraoka, K., Sorai, K., Kuno, N., et al. 2016, *PASJ*, 68, 89
- Nishimura, A., Tokuda, K., Kimura, K., et al. 2015, *ApJS*, 216, 18
- Ochsendorf, B. B., Zinnecker, H., Nayak, O., et al. 2017, *Nature Astronomy*, 1, 784
- Oka, T., Hasegawa, T., Handa, T., Hayashi, M., & Sakamoto, S. 1996, *ApJ*, 460, 334
- Oka, T., Hasegawa, T., Hayashi, M., Handa, T., & Sakamoto, S. 1998, *ApJ*, 493, 730
- Oka, T., Hasegawa, T., Sato, F., et al. 2001, *ApJ*, 562, 348
- O'Neill, T. J., Indebetouw, R., Bolatto, A. D., Madden, S. C., & Wong, T. 2022, *ApJ*, 933, 179
- Pan, H.-A., Kuno, N., Koda, J., et al. 2015, *ApJ*, 815, 59
- Papadopoulos, P., Ivison, R., Carilli, C., & Lewis, G. 2001, *Nature*, 409, 58
- Papadopoulos, P. P., van der Werf, P. P., Xilouris, E. M., et al. 2012, *MNRAS*, 426, 2601
- Paradis, D., Dobashi, K., Shimoikura, T., et al. 2012, *A&A*, 543, A103
- Pastoriza, M. G., Dottori, H. A., Terlevich, E., Terlevich, R., & Diaz, A. I. 1993, *MNRAS*, 260, 177
- Peñaloza, C. H., Clark, P. C., Glover, S. C. O., & Klessen, R. S. 2018, *MNRAS*, 475, 1508
- Peñaloza, C. H., Clark, P. C., Glover, S. C. O., Shetty, R., & Klessen, R. S. 2017, *MNRAS*, 465, 2277
- Pineda, J. L., Goldsmith, P. F., Chapman, N., et al. 2010, *ApJ*, 721, 686
- Pineda, J. L., Langer, W. D., Velusamy, T., & Goldsmith, P. F. 2013, *A&A*, 554, A103
- Pirogov, L. 1999, *A&A*, 348, 600
- Popping, G., Pérez, I., & Zurita, A. 2010, *A&A*, 521, A8
- Radford, S. J. E., Solomon, P. M., & Downes, D. 1991, *ApJ*, 368, L15
- Rafelski, M., Wolfe, A. M., Prochaska, J. X., Neeleman, M., & Mendez, A. J. 2012, *ApJ*, 755, 89
- Reid, M. J., Menten, K. M., Brunthaler, A., et al. 2014, *ApJ*, 783, 130
- Riechers, D. A., Walter, F., Carilli, C. L., et al. 2006, *ApJ*, 650, 604
- Rosolowsky, E., Hughes, A., Leroy, A. K., et al. 2021, *MNRAS*, 502, 1218
- Ruffle, P., Millar, T., Roberts, H., Lubowich, D., & Henkel, C. 2008, in *Organic Matter in Space*, ed. S. Kwok & S. Sanford, Vol. 251, 145–146
- Ruffle, P. M. E., Millar, T. J., Roberts, H., et al. 2007, *ApJ*, 671, 1766
- Sakamoto, S. 1994, *PASP*, 106, 1112
- Sakamoto, S., Hasegawa, T., Handa, T., Hayashi, M., & Oka, T. 1997, *ApJ*, 486, 276
- Sakamoto, S., Hasegawa, T., Handa, T., et al. 1999, in *Astronomical Society of the Pacific Conference Series*, Vol. 168, *New Perspectives on the Interstellar Medium*, ed. A. R. Taylor, T. L. Landecker, & G. Joncas, 90
- Sakamoto, S., Hasegawa, T., Handa, T., Oka, T., & Hayashi, M. 1996, in *Unsolved Problems of the Milky Way*, ed. L. Blitz & P. J. Teuben, Vol. 169, 501
- Sakamoto, S., Hasegawa, T., Hayashi, M., Handa, T., & Oka, T. 1995, *ApJS*, 100, 125
- Sakamoto, S., Hayashi, M., Hasegawa, T., Handa, T., & Oka, T. 1994, *ApJ*, 425, 641
- Saldaña, H. P., Rubio, M., Bolatto, A. D., et al. 2024, *A&A*, 687, A26
- Salomé, P., Combes, F., Revaz, Y., et al. 2008, *A&A*, 484, 317
- Sanders, D. B., Mazzarella, J. M., Kim, D. C., Surace, J. A., & Soifer, B. T. 2003, *AJ*, 126, 1607
- Sandstrom, K. M., Leroy, A. K., Walter, F., et al. 2013, *ApJ*, 777, 5
- Sanna, A., Reid, M. J., Dame, T. M., Menten, K. M., & Brunthaler, A. 2017, *Science*, 358, 227
- Sawada, T., Hasegawa, T., Handa, T., et al. 2001, *ApJS*, 136, 189
- Schinnerer, E. & Leroy, A. K. 2024, *ARA&A*, 62, 369
- Schöier, F. L., van der Tak, F. F. S., van Dishoeck, E. F., & Black, J. H. 2005, *A&A*, 432, 369
- Scoville, N. Z. & Solomon, P. M. 1974, *ApJ*, 187, L67
- Seta, M., Hasegawa, T., Dame, T. M., et al. 1998, *ApJ*, 505, 286
- Shan, W., Yang, J., Shi, S., et al. 2012, *IEEE Transactions on Terahertz Science and Technology*, 2, 593
- Shi, Y., Wang, J., Zhang, Z.-Y., et al. 2016, *Nature Communications*, 7, 13789
- Shimonishi, T., Izumi, N., Furuya, K., & Yasui, C. 2021, *ApJ*, 922, 206
- Sidorin, V. 2017, *Quickclump: Identify clumps within a 3D FITS datacube*, *Astrophysics Source Code Library*, record ascl:1704.006
- Sliwa, K., Wilson, C. D., Matsushita, S., et al. 2017, *ApJ*, 840, 8
- Smartt, S. J. & Rolleston, W. R. J. 1997, *ApJ*, 481, L47
- Snell, R. L., Carpenter, J. M., & Heyer, M. H. 2002, *ApJ*, 578, 229
- Solomon, P. M., Rivolo, A. R., Barrett, J., & Yahil, A. 1987, *ApJ*, 319, 730
- Sorai, K., Hasegawa, T., Booth, R. S., et al. 2001, *ApJ*, 551, 794
- Su, Y., Sun, Y., Li, C., et al. 2016, *ApJ*, 828, 59
- Su, Y., Yang, J., Zhang, S., et al. 2019, *ApJS*, 240, 9
- Sun, J., Leroy, A. K., Schrub, A., et al. 2018a, *ApJ*, 860, 172
- Sun, Y. 2015, PhD thesis, Purple Mountain Observatory, Chinese Academy of Sciences
- Sun, Y., Su, Y., Zhang, S.-B., et al. 2017, *ApJS*, 230, 17
- Sun, Y., Xu, Y., Chen, X., et al. 2018b, *ApJ*, 869, 148
- Sun, Y., Xu, Y., Yang, J., et al. 2015, *ApJ*, 798, L27
- Sun, Y., Xu, Y., Yang, J., et al. 2018c, in *Astrophysical Masers: Unlocking the Mysteries of the Universe*, ed. A. Tarchi, M. J. Reid, & P. Castangia, Vol. 336, 187–188
- Sun, Y., Yang, J., Yan, Q.-Z., et al. 2024a, *ApJS*, 275, 35
- Sun, Y., Yang, J., Zhang, S., et al. 2024b, *ApJ*, 977, L35
- Tang, X. D., Esimbek, J., Zhou, J. J., et al. 2013, *A&A*, 551, A28
- Tang, X.-D., Esimbek, J., Zhou, J.-J., Wu, G., & Okoh, D. 2014, *Research in Astronomy and Astrophysics*, 14, 959
- Tang, X. D., Henkel, C., Chen, C. H. R., et al. 2017a, *A&A*, 600, A16
- Tang, X. D., Henkel, C., Menten, K. M., et al. 2021, *A&A*, 655, A12
- Tang, X. D., Henkel, C., Menten, K. M., et al. 2019, *A&A*, 629, A6
- Tang, X. D., Henkel, C., Menten, K. M., et al. 2018a, *A&A*, 609, A16
- Tang, X. D., Henkel, C., Menten, K. M., et al. 2017b, *A&A*, 598, A30
- Tang, X. D., Henkel, C., Wyrowski, F., et al. 2018b, *A&A*, 611, A6
- Torii, K., Enokiya, R., Fukui, Y., et al. 2014, in *The Galactic Center: Feeding and Feedback in a Normal Galactic Nucleus*, ed. L. O. Sjouwerman, C. C. Lang, & J. Ott, Vol. 303, 106–108
- Tress, R. G., Sormani, M. C., Girichidis, P., et al. 2024, *arXiv e-prints*, arXiv:2403.13048
- Urquhart, J. S., König, C., Colombo, D., et al. 2024, *MNRAS*, 528, 4746
- Usuda, K. S., Hasegawa, T., Handa, T., et al. 1999, in *The Physics and Chemistry of the Interstellar Medium*, ed. V. Ossenkopf, J. Stutzki, & G. Winnewisser, 96
- Vaduvescu, O., McCall, M. L., & Richer, M. G. 2007, *AJ*, 134, 604
- van der Tak, F. F. S., Black, J. H., Schöier, F. L., Jansen, D. J., & van Dishoeck, E. F. 2007, *A&A*, 468, 627
- Wang, K., Zahorecz, S., Cunningham, M. R., et al. 2018, *Research Notes of the American Astronomical Society*, 2, 2
- Watson, L. C. & Koda, J. 2017, in *Astrophysics and Space Science Library*, Vol. 434, *Outskirts of Galaxies*, ed. J. H. Knapen, J. C. Lee, & A. Gil de Paz, 175
- Weiß, A., Walter, F., & Scoville, N. Z. 2005, *A&A*, 438, 533
- Wenger, T. V., Balser, D. S., Anderson, L. D., & Bania, T. M. 2019, *ApJ*, 887, 114
- Wiklund, T., Rydbeck, G., Hjalmarson, A., & Bergman, P. 1990, *A&A*, 232, L11
- Wild, W. 1999, *The 30m Manual: A Handbook for the IRAM 30m Telescope*
- Wilson, C. D., Howe, J. E., & Balogh, M. L. 1999, *ApJ*, 517, 174
- Wong, T., Hughes, A., Tokuda, K., et al. 2017, *ApJ*, 850, 139
- Wong, T., Oudshoorn, L., Sofovich, E., et al. 2022, *ApJ*, 932, 47
- Wouterloot, J. G. A. & Brand, J. 1989, *A&AS*, 80, 149
- Wouterloot, J. G. A. & Brand, J. 1995, in *The Physics and Chemistry of Interstellar Molecular Clouds*, ed. G. Winnewisser & G. C. Pelz, Vol. 459, 13
- Wouterloot, J. G. A. & Brand, J. 1996, *A&AS*, 119, 439
- Wouterloot, J. G. A. & Brand, J. 2005, in *Protostars and Planets V Posters*, 8214
- Wouterloot, J. G. A., Brand, J., & Fiegle, K. 1993, *A&AS*, 98, 589
- Yajima, Y., Sorai, K., Miyamoto, Y., et al. 2021, *PASJ*, 73, 257
- Yan, Y. T., Henkel, C., Kobayashi, C., et al. 2023, *A&A*, 670, A98
- Yan, Y. T., Zhang, J. S., Henkel, C., et al. 2019, *ApJ*, 877, 154
- Yang, J. 1999, *Acta Astrophysica Sinica*, 19, 55
- Yasui, C., Kobayashi, N., Tokunaga, A. T., Terada, H., & Saito, M. 2006, *ApJ*, 649, 753
- Yasui, C., Kobayashi, N., Tokunaga, A. T., Terada, H., & Saito, M. 2008, *ApJ*, 675, 443
- Yoda, T., Handa, T., Kohno, K., et al. 2010, *PASJ*, 62, 1277
- Zhang, C.-P., Li, G.-X., Zhou, C., Yuan, L., & Zhu, M. 2019, *A&A*, 631, A110
- Zhao, X., Tang, X. D., Henkel, C., et al. 2024, *A&A*, 687, A207
- Zschaechner, L. K., Bolatto, A. D., Walter, F., et al. 2018, *ApJ*, 867, 111

Appendix A: Typical structure of the Galactic edge clouds

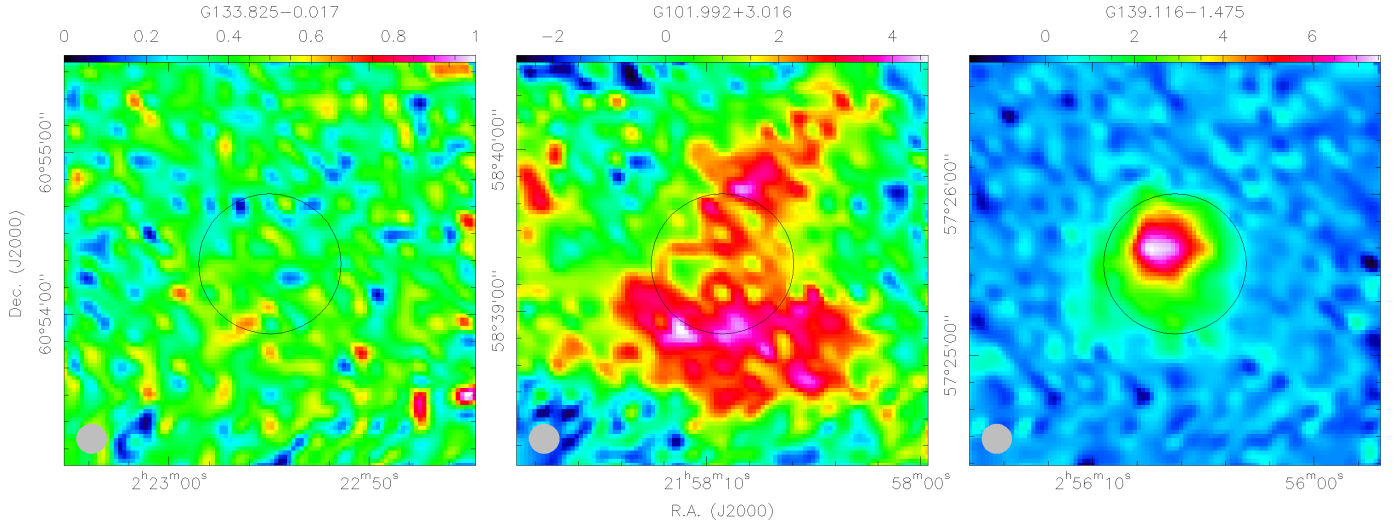


Fig. A.1. Typical velocity-integrated intensity maps of CO (2–1) for diffuse (*left*), moderate (*middle*), and compact structures (*right*) of Galactic edge clouds (T_{mb} scale; color bar in units of $K \text{ km s}^{-1}$). The black circles in the center of each map represent the CO (1–0) emission peaks identified from the Delingha 13.7 m and their size corresponds to the telescope beam size of $\sim 52''$. The grey filled circles in the lower left corner show the beam size of CO (2–1) observed with the IRAM 30 m telescope.

Appendix B: Derivation of the CO $J=2-1/1-0$ line ratio

In the context of LTE, the solution of the radiative transfer equation is formulated in a manner that involves the radiation brightness temperature of the target (Mangum & Shirley 2015)

$$T_{\text{mb}} = (1 - e^{-\tau_\nu})J_\nu(T_{\text{ex}}), \quad (\text{B.1})$$

where τ_ν represents the optical depth of the transition. A radiation temperature, often specified in the millimeter and submillimeter range, is defined as follows

$$J_\nu(T_{\text{ex}}) = \frac{h\nu}{k} \frac{1}{e^{h\nu/kT_{\text{ex}}} - 1}, \quad (\text{B.2})$$

where T_{ex} denotes the excitation temperature. h and k are the Planck and Boltzmann constants. For linear molecules, when the centrifugal stretching constant is neglected, transition frequencies are multiples of $\nu \sim 2BJ$. B is the molecular rotation constant and J represents the rotational quantum number of the upper level of the transition. The cosmic microwave background temperature is small with respect to T_{ex} and can be neglected for the sake of simplification. The brightness temperature ratio for two consecutive transitions, specifically CO (2–1) and CO (1–0), is denoted by

$$\frac{T_{\text{mb}}(2-1)}{T_{\text{mb}}(1-0)} = 2 \frac{1 - e^{-\tau_{21}} e^{\frac{h\nu_{10}}{kT_{\text{ex},10}} - 1}}{1 - e^{-\tau_{10}} e^{\frac{h\nu_{21}}{kT_{\text{ex},21}} - 1}}, \quad (\text{B.3})$$

where all indices 21 denote physical quantities associated with CO (2–1), whereas indices 10 signify physical quantities linked to CO (1–0). For example, τ_{21} and τ_{10} represent the optical depths of the CO (2–1) and CO (1–0) transitions. According to the assumption of LTE, the excitation temperature $T_{\text{ex},21}$ equals $T_{\text{ex},10}$, which in turn is equal to the kinetic temperature T_{kin} . In optically thick ($\tau_\nu \gg 1$), warm ($kT_{\text{kin}} \gg h\nu$), and dense ($n_{\text{H}_2} > 10^3 \text{ cm}^{-3}$) gas, the $T_{\text{mb}}(2-1)/T_{\text{mb}}(1-0)$ ratio approaches unity.

Under the Rayleigh-Jeans approximation ($h\nu/kT_{\text{ex}} \ll 1$), the optical depth is simply represented by

$$\tau_\nu \propto \frac{J}{2J+1} \nu n, \quad (\text{B.4})$$

where n denotes the number of molecules in a specific energy level. In a system that is in thermal equilibrium, the relative level populations adhere to the Boltzmann distribution

$$\frac{n_u}{n_l} = \frac{g_u}{g_l} e^{-\frac{h\nu}{kT}}, \quad (\text{B.5})$$

where g_l and g_u represent the degeneracy of the lower and upper energy levels of a transition, specifically $(2J+1)$ for CO. The energy separation for these two transitions are $h\nu_{10}/k_B = 5.5 \text{ K}$ and $h\nu_{21}/k_B = 11.04 \text{ K}$, respectively. In the case of optically thin emission ($\tau_\nu \ll 1$), Eq. B.3 can be reduced to

$$\frac{T_{\text{mb}}(2-1)}{T_{\text{mb}}(1-0)} \approx \frac{\tau_{21}}{\tau_{10}} \approx 4e^{-\frac{11.04}{T_{\text{ex},21}}}, \quad (\text{B.6})$$

implying that the $T_{\text{mb}}(2-1)/T_{\text{mb}}(1-0)$ ratio can potentially attain a value as high as four in dense, warm, and optically thin gas. The $T_{\text{mb}}(2-1)/T_{\text{mb}}(1-0)$ ratio exhibits an exponential dependence on the excitation temperature at low temperatures. This ratio may approach unity under optically thick conditions, while it may reach values up to four in optically thin conditions. These conclusions are also valid for the R_{21} ratio of velocity integrated intensities, if both transitions have the same line widths.